Unmixing river sediments for the elemental geochemistry of their source regions

Submitted, non-peer reviewed manuscript, compiled April 15, 2021

Alex G. Lipp[1*], Gareth G. Roberts[1], Alexander C. Whittaker[1], Charles. J. B. Gowing[2], and Victoria M. Fernandes[1]

[1]Department of Earth Sciences and Engineering, Imperial College London, UK
[2]Centre for Environmental Geochemistry, British Geological Survey, Keyworth, UK

Abstract

The geochemistry of river sediments is routinely used to obtain information about geologic and environmental processes occurring upstream. For example, downstream samples are used to constrain chemical weathering and physical erosion rates, as well as the locations of mineral deposits or contaminant sources. Previous work has shown that, by assuming conservative mixing, the geochemistry of downstream samples can be reliably predicted given a known source region geochemistry. In this study we tackle the inverse problem and 'unmix' the composition of downstream river sediments to produce geochemical maps of drainage basins (i.e., source regions). The scheme is tested in a case study of rivers draining the Cairngorms, UK. The elemental geochemistry of the < 150 μm fraction of 67 samples gathered from the beds of channels in this region is used to invert for concentrations of major and trace elements upstream. We solve this inverse problem using the Nelder-Mead optimisation algorithm and by seeking only spatially smooth maps. The best-fitting source region geochemistry for 20 elements of different affinities (e.g., Be, Li, Mg, Ca, Rb, U, V) is assessed using independent geochemical survey data. The inverse approach makes reliable predictions of the major and trace element concentration in first order river sediments. We suggest this scheme could be a novel means to generate geochemical baselines across drainage basins and within river channels.

***K*eywords** Sedimentary geochemistry · Inverse modelling · Mixing · Geochemical mapping · Fluvial Geomorphology

1 Introduction

Sediments contained in river channels are the products of physical and chemical weathering of rocks outcropping in the upstream drainage basin (Weltje and Eynatten 2004; Weltje 2012; Caracciolo 2020). During transport, sediment geochemistry is also altered by processes including weathering, sorting and cation-exchange (Bouchez et al. 2011, 2012; Tipper et al. 2021). As fluvial sediments can be transported on relatively long timescales, of order 10^2 – 10^3 yr, their geochemistry represents a spatially and temporally integrated signal of catchment processes (Repasch et al. 2020). They are therefore frequently studied to understand the rates and location of chemical weathering, physical erosion and sediment transport (e.g., Canfield 1997; Gaillardet et al. 1999; Riebe et al. 2003; Viers et al. 2009; Garzanti et al. 2012; Lupker et al. 2012, 2013; Garzanti et al. 2014; Schneider et al. 2016; Ercolani et al. 2019). However, given that geochemical mixing, in-transit modification or selective deposition may take place, the extent to which downstream river sediment geochemistry contains the desired source region signal remains challenging to quantify. An objective scheme which translates downstream sediment geochemistry into that of the corresponding upstream source-region is therefore desirable. Such a scheme would produce predictions of the upstream geochemistry which can be used investigate controls on Earth surface processes, but without the unwanted effects of mixing. Moreover, such a scheme would allow the effects of other proposed in-transit processes (e.g., weathering in-transit) to be quantified. Proposing and testing such an 'unmixing' scheme is the goal of this study.

River sediment geochemistry is also widely used as a medium for geochemical surveys which provide valuable data for mineral resource exploration, environmental monitoring and wider geologic understanding (Garrett et al. 2008). The understanding of river sediment geochemistry is therefore also significant from an applied and economic geochemistry perspective. As sediments in streams integrate the geochemistry of their entire catchment, sampling them is a more resource efficient way to survey large areas than sampling, for instance, soils or outcropping rocks. Depending on practical constraints however, the size of the sampled catchment can vary over orders of magnitude. For example, the National Geochemical Survey of Australia samples catchments with areas ~ 5000 km^2, whereas the analogous national survey of the UK typically samples catchments with upstream area generally less than 100 km^2 (Caritat and Cooper 2016; Johnson et al. 2018b). Understanding precisely how the geochemical signal of source regions propagates downstream in sediments, and how it can be recovered from samples downstream, would allow better understanding of the trade-offs involved in surveying catchments of different areas. This in turn would better inform subsequent sampling campaigns.

1.1 *Study design*

Our study design is illustrated by the schematic in Figure 1. Consider a river catchment that contains three geochemical endmembers which could correspond to, e.g., lithologic units. These endmembers are represented as the red, green and blue areas in Figure 1. The sediment in rivers draining each of these regions inherits the geochemistry of these sediment sources, as indi-

*correspondence: a.lipp18@imperial.ac.uk

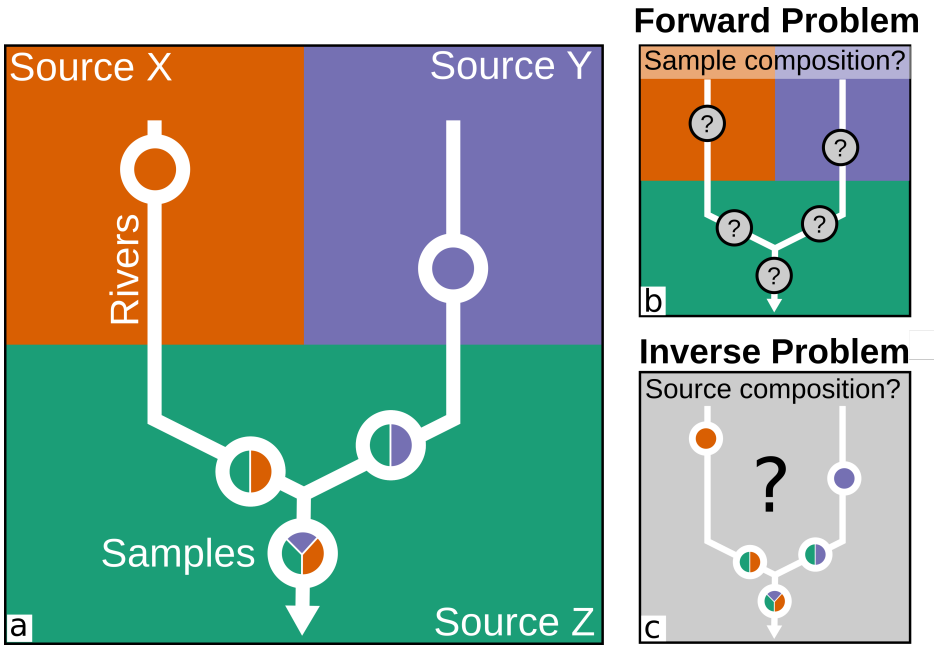

Figure 1: **Predicting provenance: Composition of sediments in rivers and upstream sources from forward and inverse modelling.** (a) Schematic showing composition of source regions (X, Y, Z), drainage network (white lines) and composition of sampled river sediments (white circles). In this simple scheme composition of sediment in rivers (e.g., colored pie charts) is determined by the composition of upstream source regions. (b) Schematic shows the forward, 'mixing', problem when the source region geochemistry is known and the downstream composition at sample sites is predicted (see Lipp et al. 2020). (c) The inverse, 'unmixing', problem attempts to reconstruct the composition of source regions from the point observations of downstream sediment composition, which is the focus of this study.

cated in Figure 1 by the pie charts representing the contributions from each endmember. Downstream geochemistry changes as tributaries draining different sources join or the river erodes a different source region. The 'forward' problem, as we define it here, is to predict the composition of sediment at sample sites downstream given the spatial distribution of geochemistry in source regions and a known drainage network (Figure 1b). An example of this forward problem was implemented and successfully validated in Lipp et al. (2020). The 'inverse' problem addressed in this paper seeks unknown source region composition by inverting the known sediment compositions at the sample sites downstream (Figure 1c).

In this manuscript we consider the 'source region geochemistry' to mean the elemental composition of river sediments in the most upstream portion of the drainage network, i.e., first order streams. We recognise that other definitions of source region geochemistry may be used, most obviously the composition of the underlying bedrock lithology. We use the geochemistry of stream sediments as our target as opposed to the bedrock as stream sediments have already undergone chemical weathering on hillslopes prior to entering the drainage network. Stream sediment geochemistry is also strongly influenced by the underlying bedrock (see e.g.,Kirkwood et al. 2016). Stream sediments hence incorporate geochemical information about both lithology and weathering whereas bedrock can only inform about lithology.

Given the ubiquity of mixing in the Earth sciences, a number of quantitative unmixing procedures have been previously developed. The most general case of unmixing is where both the endmembers (i.e., the compositions that are being mixed) and the mixing proportions are sought, so as to explain variability in a proposed mixture dataset. Weltje (1997) developed a numerical solution to this general problem which has been used to model a range of different datatypes including fossil abundances, rock magnetism and grain size distributions (Dam and Weltje 1999; Weltje and Prins 2007; Dekkers 2012). In the instance where the endmembers are assumed to be known, calculating the mixing proportions is relatively straightforward, and frequently solved on an ad hoc basis or as part of a Bayesian framework (e.g., Stock et al. 2018). The unmixing problem we consider differs in that we explicitly seek the spatial structure of both the endmembers and the mixture, i.e., geochemical maps of source regions and the composition of downstream river sediment samples, respectively. This approach is most similar to that developed by De Doncker et al. (2020). They sought the spatial pattern of erosion in a catchment through a Bayesian inverse of downstream sediment tracers. We, instead, seek the composition of source regions given mixing proportions calculated using drainage networks.

1.2 Outline

In this study, we first introduce the study area in the Cairngorms, UK, where we demonstrate the approach. We describe how 67 samples of bed material were gathered from trunk channels and tributaries along the five major river basins in the area. An implementation of the forward problem for these drainage basins is described in Lipp et al. (2020). We then present a quantitative procedure that uses the structure of drainage networks to convert

maps of source region geochemistry into predictions of downstream sediment geochemistry at sample sites. A formal inverse problem is then posed, in which the unknown geochemistry of source regions is sought. We describe how this problem can be solved by inverting downstream samples by optimisation of a regularised objective function. The fidelity of predicted source compositions generated from this inverse procedure is assessed by recovery of known synthetic inputs. We then present the results of inverting real geochemical data from downstream sediment samples for different geochemical elements. Finally, these results are evaluated using independent geochemical survey data from the study region.

1.3 Study area

We focus our study on five rivers draining the Cairngorms mountains, Scotland, UK: Dee, Deveron, Tay, Don and Spey (Figure 2a). River sediments were extracted from these channels at 67 sample sites indicated in Figure 2b–c. Sediments within these rivers have been previously analysed by Lipp et al. (2020), where it was demonstrated that the forward problem described in Figure 1 can be used to make accurate predictions of downstream river geochemistry. This successful demonstration of the forward model means that these same rivers are excellent candidates to explore the use of inverse modelling. The region has also been geochemically mapped by the Geochemical Baseline Survey of the Environment (G-BASE), a geochemical survey conducted by the British Geological Survey (Johnson et al. 2005; sample sites shown in Figure 2d). As a result, there is a pre-existing independent dataset that can be used to test predictions from inverse modelling. We chose this region for three reasons. First, for the UK, it has relatively high topographic relief and a high natural sedimentary flux. Second, a significant portion of the region is in a protected national park limiting potential anthropogenic effects. Finally, this region contains a variety of lithologic units and substrate compositions including mafic and felsic igneous intrusions hosted within meta-sedimentary units (Figure 3a).

2 DATA & METHODS

2.1 Upstream source region geochemistry

We will test predicted source compositions using the independent G-BASE geochemical survey data. G-BASE sampled the fine-grained, $< 150\ \mu$m, fraction of low-order stream sediments (i.e., those with very small upstream areas) with an average sampling density of 1 *per* 2 km^2. These sediment samples were subsequently analysed for a range of geochemical analytes. In the study region this analysis was performed principally by Direct Reading Optical Emission Spectrometry, with the exception of uranium which was analysed by Delayed Neutron Activation. The sampling and geochemical analytic procedure used by G-BASE, as well as quality control measures, are described by Johnson et al. (2018a,b).

The G-BASE stream sediment geochemical survey, like other high sample density surveys, primarily reflect geochemicals variations in the underlying bedrock (Everett et al. 2019). This lithological control on geochemical survey data is also clearly displayed in our study region. Figure 3a displays the geological map of our study area. Figures 3b-d indicate the concentration of magnesium, potassium and titanium respectively in stream sediments from the G-BASE dataset. These geochemical maps indicate the strong relationship between stream sediment geochemistry and the underlying lithology (Figure 3a). For example, the felsic intrusions at the centre of our region are low in Mg and Ti but enriched in K.

We can explore the geochemical variability of the region better using Principal Component Analysis (PCA), a multivariate tool frequently applied to geochemical survey data (e.g., Kirkwood et al. 2016). PCA rotates multi-dimensional data onto a smaller number of principal components (PCs) along which variance is maximised. This rotation therefore simplifies a dataset. Full details of this multivariate method are given in the methods. Figure 3e displays the first three PCs of 22 elements from the G-BASE dataset in a red-green-blue (RGB) ternary space (Figure 3f), where the RGB channels correspond to the (normalised exponents of the) first, second and third PCs respectively. This figure therefore displays the principal geochemical domains of the region. The first PC corresponds to relative enrichment in felsic associated elements (e.g., U, Be, Rb) and defines the felsic intrusions at the centre of the study region. The second PC corresponds to an enrichment in certain metals (e.g., Pb, Cu, Li) and appears to demarcate the different sedimentary units. The third PC corresponds to relative enrichment in some alkaline earths (Sr, Ca, Ba) and identifies the mafic intrusions in the NE of the study area. The goal of our inverse modelling is to reconstruct these principal geochemical domains using just a small number of sediment samples gathered from localities downstream.

2.2 Downstream sediment geochemistry

The $< 150\ \mu$m fraction of bed material was gathered from localities on the studied rivers and their geochemistry was measured following G-BASE protocols. This dataset was first reported in Lipp et al. (2020). In total, 67 samples were gathered from 63 sample sites (Figure 2b). The sample sites divide the study area into a series of nested sub-catchments, which are displayed in Figure 2c. Sampling density means that the majority of sub-catchments have areas 200–400 km^2. In the southern portion of the Tay catchment lower sampling density results in sub-catchments with greater areas (Figure 2c).

At four localities duplicate samples were extracted to investigate local geochemical heterogeneity. Statistical analysis of the duplicate samples, reported in Lipp et al. (2020), indicated that the vast majority of the geochemical variability in these samples reflects variation between sample sites, not local heterogeneity. Whilst a larger suite of elements was gathered, we focus on the following 22 elements, which are present in the downstream samples and were measured consistently by G-BASE in the study area: Ba, Be, Ca, Co, Cr, Cu, Fe, K, La, Li, Mg, Mn, Ni, Pb, Rb, Sr, Ti, U, V, Y, Zn and Zr. This subset was selected so that predictions from the inverse model can be evaluated using the independent G-BASE dataset.

The sampling procedure we used replicated the standard G-BASE sampling protocol. This replication makes the data gathered directly comparable between the two datasets. bed material was extracted from the river channel by shovel and deposited on a sieve-stack. First, a 2 cm grill was used to remove pebbles. The material was then rubbed through a 2 mm and then 150

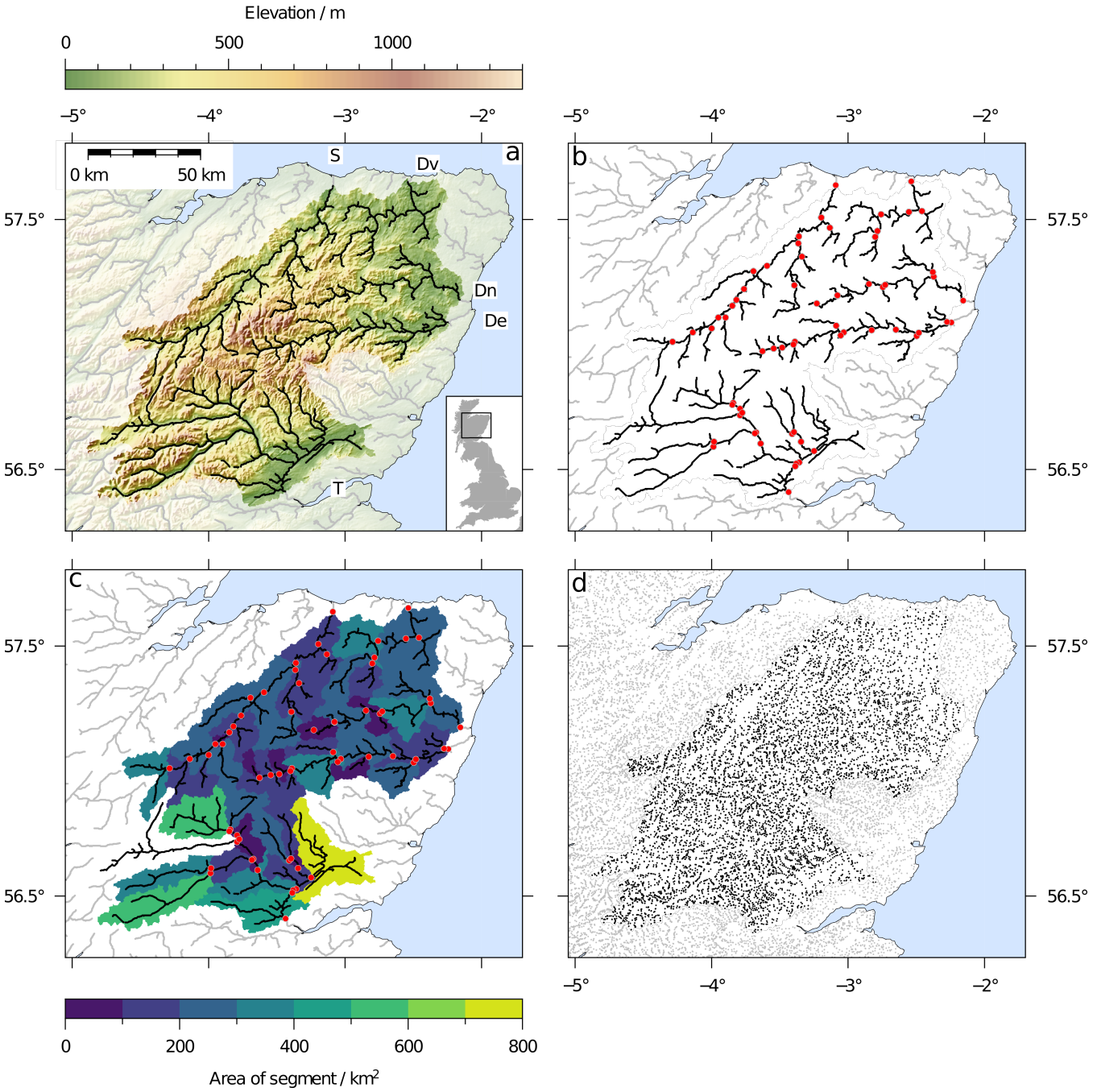

Figure 2: **Introduction to study area: Cairngorms, UK**. (a) Topography from SRTM1s digital elevation model. Transparent overlay indicates region outside the five studied river catchments. Black lines = river channels with upstream area > 25 km^2. Rivers labelled: S = Spey, Dv = Deveron, Dn = Don, De = Dee, T = Tay. Inset shows location of study area. (b) Location of 67 sediment sample sites (red circles) on river channels used to predict the composition of upstream source regions. (c) Unique drainage area segments corresponding to each sample site; color indicates area of sub-catchment, which approximates effective resolution of the inverse model (see body text). (d) Black points = G-BASE geochemical survey sample sites, which are used to test the accuracy of predicted source region chemistry. Gray points lie outside of studied catchments.

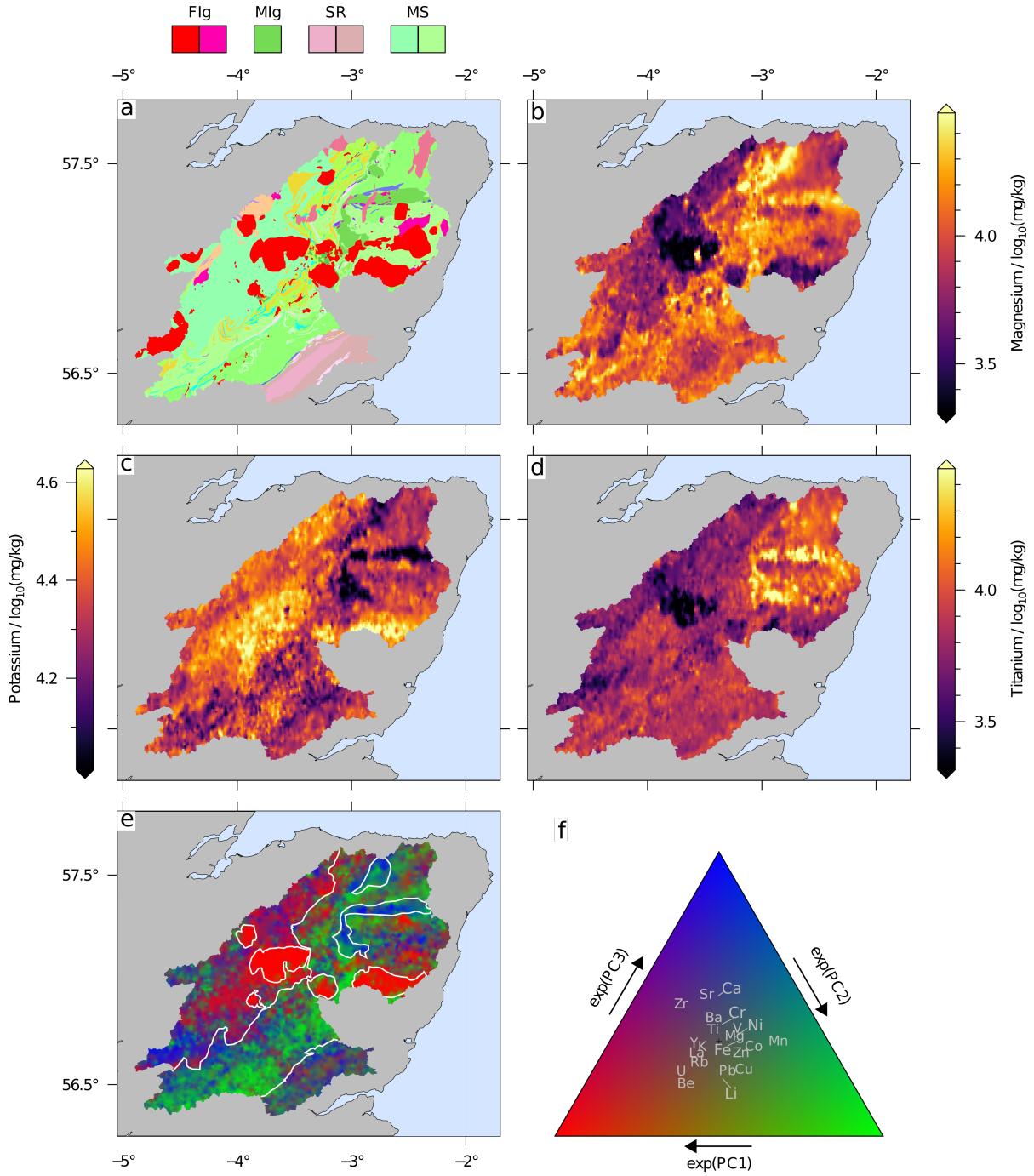

Figure 3: **Geology and geochemistry of Cairngorms.** (a) Geologic map of studied area, reproduced with the permission of the British Geological Survey UKRI, all rights reserved. Major lithologies indicated: Flg = Ordovician to Devonian felsic igneous intrusions; Mlg = Ordovician to Silurian mafic igneous intrusions; SR = Sedimentary rocks, mostly Devonian sandstones; MS = Metasedimentary rocks, mostly Neoproterozoic psammites. See mapapps.bgs.ac.uk/geologyofbritain/home.html for full geologic key. (b) Concentration of magnesium in first-order stream sediments from G-BASE survey. Note relationship to lithology shown in panel (a) and similar spatial structure to other elements displayed in panels (c–e). (c) Potassium. (d) Titanium. (e) Principal component map for 22 elements in G-BASE dataset following a centred log-ratio transformation (Aitchison 1983). The first three principal components of the dataset are extracted and converted into a red-green-blue ternary space, which highlights the major geochemical domains in the study region. White lines indicate simplified lithological map to highlight key geochemical domains. See panel (f) for key. (f) Ternary plot showing relationship between colour, principal components and geochemistry. Reds and greens indicate compositions that are relatively enriched in elements such as U, Be, Rb indicating felsic association and metallic elements (e.g., Li, Pb, Cu, Co), respectively; blues indicate relative enrichment in alkaline earth elements (e.g., Ca, Sr, Ba). The displayed principal components explain 62.1 % of the total variance.

μm nylon sieve into a fiberglass collecting pan. After letting suspended sediment settle out for ~ 15 minutes, excess water was decanted, and the homogenised sediment slurry was poured into a reinforced paper bag. Each paper bag was placed within a sealed plastic bag to prevent contamination. The bagged sediment samples were air-dried until they had the consistency of modelling clay, before being freeze-dried for short-term storage prior to geochemical analysis.

The freeze-dried sediments were powderised in an agate ball mill and homogenised, and an analytical subsample taken by cone-quartering. For each geochemical analysis 0.25 g of powder was accurately weighted into Savillex tubes. The powders were digested using HF, HNO_3 and $HClO_4$ on a hotplate. Comparison to standards indicated that some elements hosted in resistate minerals (e.g., Zr) were, as expected from this method, only partially digested at this stage. Post-digestion the sample was resolubilised using HNO_3 and H_2O_2, and analysed for a full suite of elements using an Agilent 8900 Inductively Coupled Plasma Mass Spectrometer at the British Geological Survey.

2.3 Topographic data and processing

For our inverse scheme we require the drainage-network of the region to be defined. We opt to extract drainage automatically from topographic data using widely-used algorithms. Drainage networks were extracted from the SRTM1s topographic dataset down-sampled to a square grid with resolution 200 × 200 m. Prior to down-sampling the data underwent a cylindrical equal-area projection centred on the study area using GMT 6.0.0 (Farr et al. 2007; Wessel et al. 2013). Depressions in the digital elevation model were then filled use the 'priority-flood' algorithm (Barnes et al. 2014). Subsequently, drainage networks were extracted from this DEM using the 'D8' flow-routing algorithm, which allows drainage area to be defined at every point in the model grid (O'Callaghan and Mark 1984). The location of major channels, i.e., cells with upstream area > 25 km^2 are shown in Figure 2a-c. All landscape modelling calculations were performed using the LandLab 2.2.0 package for python 3.8.5 (Van Rossum and Drake 2009; Barnhart et al. 2020). The resulting extracted drainage networks are displayed throughout the manuscript (e.g., Figure 2a–c).

2.4 Principal Component Analysis

PCA is used in this study to investigate relationships between elements and to identify spatial geochemical domains. PCA is a very widely used technique to simplify high-dimensional datasets. As geochemical datasets are compositional in nature (i.e., strictly positive data that sum to a constant) a log-ratio transformation must be applied prior to application of PCA. In this instance we use the centred log-ratio transformation (Aitchison 1983). We apply PCA to both the G-BASE datasets and our inverse solutions. We use the implementation of PCA in the scikit-learn package for python which uses singular value decomposition to define the principal components (Pedregosa et al. 2011).

To visualise three PCs simultaneously on one map we transform them onto an RGB mixing ternary (e.g., Figure 3e–f) as follows. The scores on the first three PCs are calculated, raised to an exponent and then normalised by the sum of these three exponentials. The resulting values (which sum to one) are then used to weight the red, green and blue channels respectively for visualisation.

3 Forward and Inverse Modelling

3.1 Forward model

Here we describe the procedure to predict downstream sediment geochemistry given a known distribution of geochemistry and topography in the source-region. The forward model as described here has been implemented and succesfully tested for this region previously (Lipp et al. 2020). Let $C(x, y)$ be the concentration of some element in the sediment source regions of a drainage network, e.g., magnesium. C can be approximated by geochemical surveying, e.g., Figure 3b-d. We seek to predict D which is the concentration of that same element in downstream river-sediments at a point in a river which has an upstream drainage area 'A'. The concentration downstream, D, is simply the sum of the contributions to this element from every upstream point in the basin, A, normalised to the total sediment flux. If A has a spatially varying erosion/surface-lowering rate, $\frac{\partial z}{\partial t}$, then each point in A contributes $\frac{\partial z}{\partial t} \times C$ amount of the target element, i.e., the total amount of sediment produced by that point, multiplied by the concentration of the element in question. The total sedimentary flux is the total amount of erosion occurring upstream, i.e., $\int_A \frac{\partial z}{\partial t} \mathrm{d}A$. Combining these relationships provides the following estimate of concentration in downstream samples

$$D = \frac{1}{\int_A \frac{\partial z}{\partial t} \mathrm{d}A} \int_A \frac{\partial z}{\partial t} C \, \mathrm{d}A. \tag{1}$$

Under this formulation the concentration of element in sediment downstream can be predicted if the erosion rate and concentration can be defined at all points in the upstream region, assuming instantaneous sediment transport and no in-transit chemical modification (e.g., Sharman et al. 2019; De Doncker et al. 2020). This approach assumes that all chemical weathering happens in-situ (e.g., on hillslopes) before sediments enter the fluvial system.

An unknown in this formulation is erosion rate, $\partial z/\partial t$. As $\partial z/\partial t$ is required to be defined continuously across the studied region, a reasonable approach is to use landscape evolution models. The widely-used stream power model, for example, predicts erosion rates using empirical relationships between slope angle, upstream area and erosion rate (see e.g., Howard and Kerby 1983; Tucker and Whipple 2002). In Lipp et al. (2020) the stream power model was used to predict erosion rates and hence composition of sediment downstream using Equation 1 for the same data-set used here. Changing model parameters had a minor effect on the goodness-of-fit for downstream data. In fact, spatially homogenous incision (i.e., constant $\partial z/\partial t$) was found to provide, by a small margin, the best fit to the data downstream. These results, combined with the results of tests in which substrate was varied, indicated that downstream geochemistry was much more sensitive to the drainage network topology and source region geochemistry. Hence, in this study we proceed with this assumption of homogeneous incision. The validity of this assumption of spatially constant incision will be

implicitly tested when predictions from inverse modelling are compared to independent data.

Under the assumption of homogenous incision (i.e., $\partial z/\partial t = k$, where k is a constant), Equation 1 can be simplified further to give

$$D(x, y) = F(C) = \frac{1}{|A|} \int_A C \, \mathrm{d}A. \tag{2}$$

This simply states that the composition of sediment downstream, D, is an equal area weighted mixture of the composition of its upstream region. In summary, Equation 2 is the forward model, $F(C)$, we use to transform a spatial map of upstream geochemistry, $C(x, y)$, into a prediction of sediment geochemistry downstream, $D(x, y)$. Figure 4 shows solutions to this forward problem. In this example the mapped concentration of Mg from G-BASE (Figure 3b) is used as C and input into the forward model to predict the downstream sediment concentration, $D = F(C)$. This predicted downstream concentration is shown in Figure 4a with the true observations overlain.

3.2 Defining the inverse model

3.2.1 Traversing model space

The goal of the inverse procedure is to identify the upstream geochemistry, C, that best fits point observations downstream. Here we describe a procedure for systematically and objectively exploring different possible values of C. We discretise C onto a grid of $x \times y$ resolution 5×5 km. Thus C is represented as a vector, $\mathbf{C}$, of length equal to the number of grid-cells contained within or overlapping our studied drainage area, which for our chosen resolution is 601. This discrete vector can be converted into a continuous map of geochemistry, C, by upsampling onto the resolution of the base DEM we use (200×200 m). This upsampled C can then be fed into the forward model.

Instead of seeking the vector $\mathbf{C}$ directly, we instead seek the vector $\log(\mathbf{C})$, which we term $\mathbf{C}'$. We seek $\log(\mathbf{C})$ as the information contained in geochemical data is relative, not absolute (Aitchison 1986; Pawlowsky-Glahn and Egozcue 2006). For example, consider the change in concentration of some trace-element from 0.01 wt% to 1 wt%. This is a significant relative change of 100 times the original value, but an absolute change of only 0.99 wt%. If that same element changes in concentration again to 2 wt%, the relative change is only two times the intermediate value, much smaller than the initial change. However, the absolute change is in fact larger, i.e., 1 wt%. Given that elemental concentrations frequently traverse many orders of magnitude, our cost function must be sensitive to relative not absolute changes in concentration. In logarithmic space, the first change in concentration is correctly identified as traversing a greater compositional distance than the second change, hence its application here.

We note that as compositional data is strictly bounded between 0 and some closure value (e.g., 100 %, 10^6 ppm etc...), the sigmoidal logit function should be used instead of a log function. However, given that the elements we analyse here are all generally < 10 wt%, where the logit and log functions are functionally identical, we use a log function as it is computationally faster to calculate.

3.2.2 Data misfit

We seek the upstream geochemistry vector, $\mathbf{C}$, that best explains the observations of concentration downstream which we represent as a vector, $\mathbf{D}_{obs}$. This vector has length 67, equal to the number of observations we have made. For each observation, there is a corresponding predicted concentration, which is simply the value of $F(C)$ evaluated at the sample site. We represent these predictions, for a given C, as the vector $\mathbf{F}(C)$. We need to formally define a metric that quantifies the difference between the predicted, $\mathbf{F}(C)$, and observed, $\mathbf{D}_{obs}$, sediment concentrations. For this, we use the square of the Euclidean norm of the difference between the values, after a logarithmic transform, i.e.,

$$\left\| \log\{\mathbf{F}(C)\} - \log\{\mathbf{D}_{obs}\} \right\|^2 = \sum_i \left[\log\{F(C)_i\} - \log\{D_{obs,i}\} \right]^2. \tag{3}$$

We utilise the logarithmic transform prior to calculating the misfit, again, due to the relative nature of information in compositional data. A visualisation of the misfit between and observed and predicted concentrations is shown in Figure 4b.

3.2.3 Regularisation

This inverse problem is likely to always be underdetermined (i.e., there are fewer observations than free parameters). In the example we consider there are almost an order of magnitude more unknown compositions (upstream source) than known compositions (downstream samples). Underdetermined problems are often solved by imposing constraints on properties of the solution, e.g., minimising roughness (Parker 1994). In this instance, we seek smooth geochemical maps that best fit the composition of the 67 downstream samples. We do so by penalising the roughness of upstream geochemistry, C. We formally define roughness here as the sum of the square of the Euclidean norms of the first derivative of C' in both the x and y directions, i.e.,

$$\left\| \frac{\partial C'}{\partial x} \right\|^2 + \left\| \frac{\partial C'}{\partial y} \right\|^2. \tag{4}$$

To quantify the first-derivative we calculate the first discrete difference between adjacent values of the, logarithmic, $\mathbf{C}'$ grid in both the x and y directions, assuming Von Neumann boundary conditions that are equal to zero (i.e., $\partial C'/\partial x = \partial C'/\partial y = 0$).

3.2.4 Optimising the objective function

Considering both the data-misfit and roughness constraints, the best fitting source-region chemistry is that which minimises the following objective function, $X(\mathbf{C}')$:

$$X(\mathbf{C}') = \overbrace{\left\| \log\{F(\mathbf{C})\} - \log\{\mathbf{D}_{obs}\} \right\|^2}^{\text{Data Misfit}} + \lambda^2 \overbrace{\left(\left\| \frac{\partial \mathbf{C}'}{\partial x} \right\|^2 + \left\| \frac{\partial \mathbf{C}'}{\partial y} \right\|^2 \right)}^{\text{Roughness}}. \tag{5}$$

As we, strictly speaking, seek $\log(\mathbf{C})$, which must be raised to an exponent prior to being entered into the forward model, this is a non-linear inverse problem.

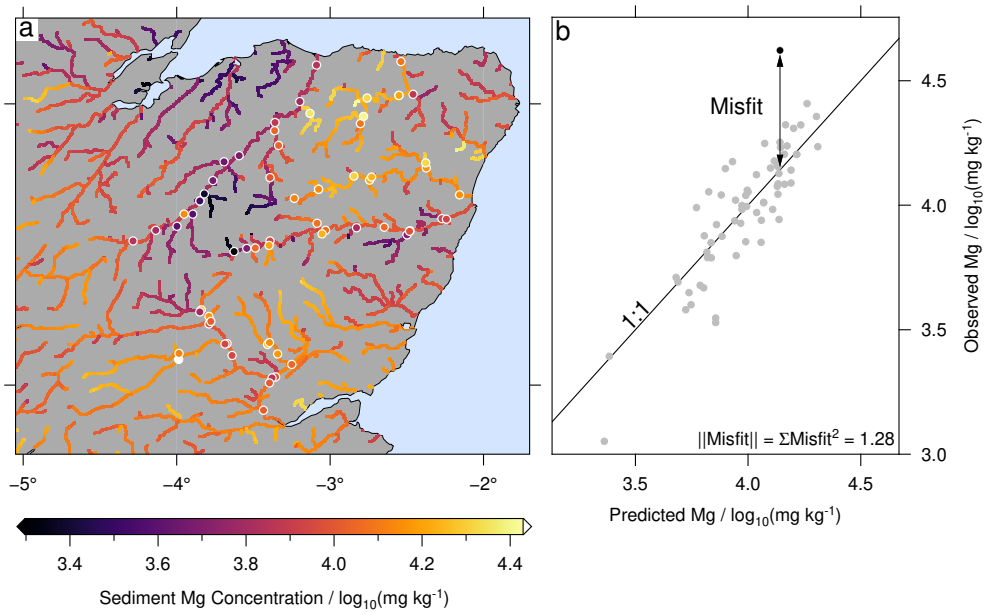

Figure 4: **Predicting chemistry downstream: Example of solving the forward problem**. (a) Coloured lines show predicted concentration (C) of magnesium along rivers generated by integrating magnesium concentrations from the G-BASE survey with respect to distance downstream (Figure 3b; see body text). Coloured circles are 67 independent spot measurements of magnesium concentration in river-sediments (see Lipp et al. 2020). (b) Cross-plot of observed, $\mathbf{F}(C)$, and predicted, $\mathbf{D}_{obs}$, magnesium concentration at the 67 sample sites. Black line = 1:1 relationship. Global misfit (1.28) is the summed squared differences between the logarithm of $\mathbf{F}(C)$ and $\mathbf{D}_{obs}$ (see body text; e.g., double-headed arrow).

The parameter λ is the smoothness coefficient that controls the extent to which roughness is penalised. λ is a hyper-parameter that must be manually set for each element. High values of λ result in solutions which are spatially very smooth but fit the data poorly (underfitting). Conversely, very low values of λ result in very good fits to the data but resultant maps of C which are geologically implausible due to their spatial roughness (overfitting). Hence, λ is chosen based on this trade-off between roughness and data-misfit. We use the 'elbow' method of Parker (1994), where many values of λ are tried and the optimal λ is chosen such that it lies at the maximum curvature of a data-misfit against roughness plot.

Assuming that there is no analytic solution for the minima of X we minimise Equation 5 numerically. We minimise X, with respect to $\mathbf{C}'$, using Gao and Han (2012)'s implementation of the Nelder-Mead algorithm using SciPy libraries (Virtanen et al. 2020). The Nelder-Mead algorithm, also known as the downhill simplex method, works by generating a series of multidimensional simplexes (the 2D simplex is a triangle, the 3D simplex is a tetrahedron etc.) that by a series of reflections, expansions and contractions brackets the minimum of the objective function with an increasingly tight radius (see e.g., Press et al. 1992). The algorithm finishes when the absolute change in the objective function and the maximum change of any parameter at each iteration cycle is less than a specified tolerance. Both these criteria must be met for convergence. We use an absolute finishing tolerance for both X and $\mathbf{C}'$ of 10^{-4}. As an initial starting condition for $\mathbf{C}'$ we assume a homogenous composition equal to the upstream-area weighted average composition of the samples extracted from the most downstream samples of each of the five rivers. The number of iterations required to converge to a solution is generally of the order 10^5–10^6 depending on the element and λ value chosen. On the authors' standard desktop with Intel i7 processor at 2.5 GHz this takes on the order of 10^1 - 10^2 hours to converge. A Jupyter notebook containing python implementations all of the calculations described above is provided (see Data Availability Statement).

4 RESULTS

4.1 Synthetic Examples

First we explore the extent to which this inverse scheme can recover a known, synthetic input. Figure 5a displays a synthetic source-region geochemistry for an arbitrary geochemical element. This 'chequerboard' pattern has a peak-to-trough distance of 40 km. From this synthetic input we then calculate the composition of downstream samples, which become the 'observations' used to invert for a source composition (Equations 2 & 5). We invert 67 'observations' at locations corresponding to the actual sample locations along the Spey, Deveron, Dee, Don and Tay rivers. If the inverse scheme is working correctly, the best fitting C should approximate the input map displayed in Figure 5a.

Comparing Figure 5b to Figure 5a it is clear that the inverse scheme is successfully able to largely recover the location and amplitude of geochemistry in sediment source regions. We emphasise that this input was recovered using just the 67 (synthetic) observations at the sample sites (red dots in Figure 5b). The 'pixelation' in Figure 5b is a result of the discretization of C, discussed above, but does not prevent the scheme from resolving the significant spatial signals. The best-fitting solution to

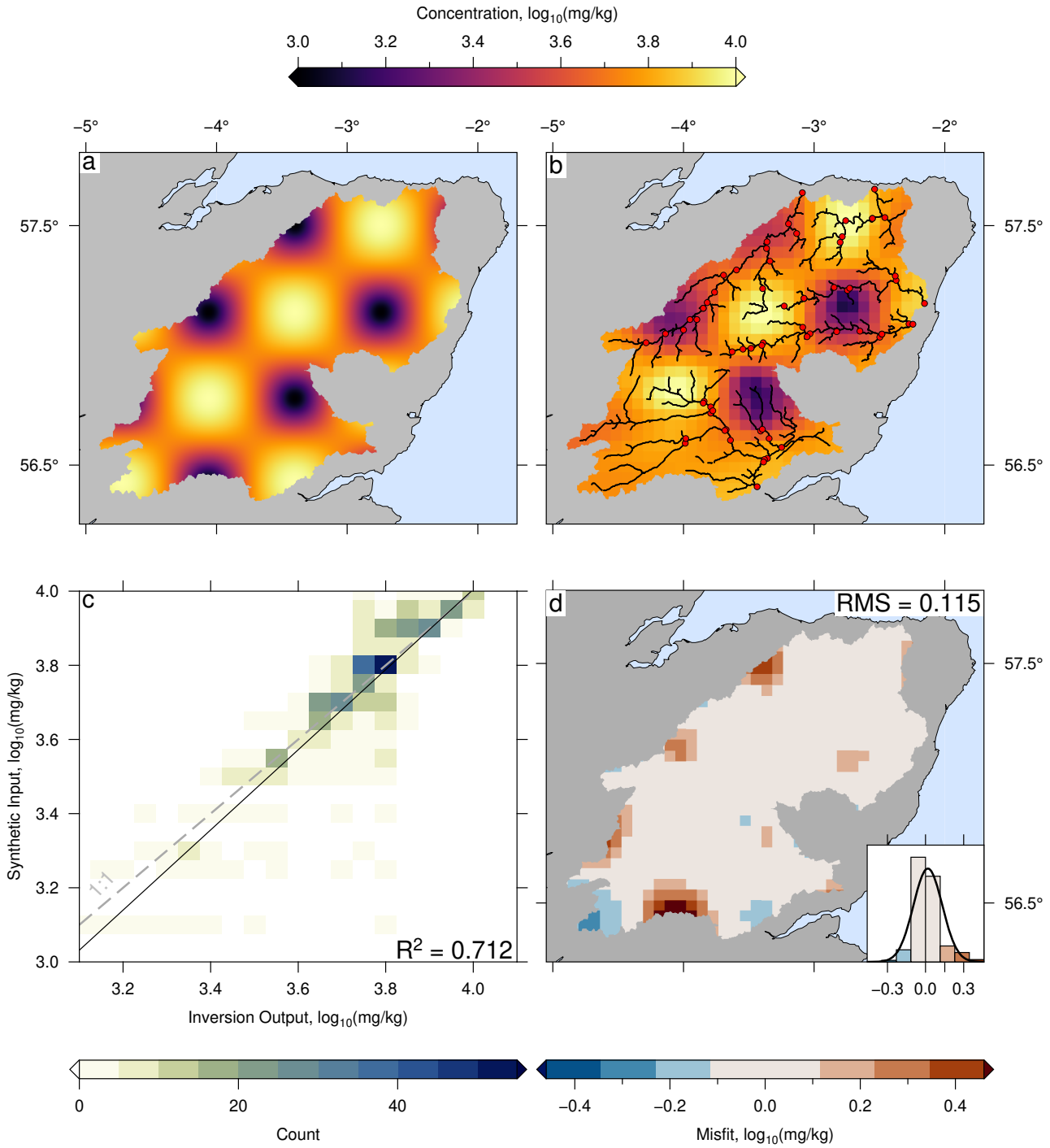

Figure 5: **Predicting geochemistry upstream: An example of solving the inverse problem**. In this example we test the fidelity of the inverse model by inverting for a synthetic (i.e., completely known) source composition using real rivers and positions of actual sample sites. (a) Synthetic elemental concentration map generated using a 2D sine function (peak to trough = 40 km). This map was used to calculate sediment concentrations at sample sites (red circles in panel b), which were inverted for source composition. (b) Predicted source composition calculated by inverting synthetic compositions at the 67 sample sites (red circles). In this example smoothing parameter $\lambda = 10^{-0.5}$. (c) 2D histogram of observed and predicted source concentrations; the grid resolution of observed and predicted composition is 5×5 km (see panel b). 1:1 relationship is shown by gray dashed line; black solid line = linear regression. (d) Misfit between observed and predicted source composition. Color bar is discretised on intervals equal to global RMS misfit. Misfit is highest in regions of low sample coverage (see Figure 2c). Inset shows histogram of misfits with binwidth = global RMS misfit; Best fitting normal distribution (black curve) is shown for comparison. Analogous figures for synthetic inputs with different input wavelengths are given in Supplementary Figure S-1.

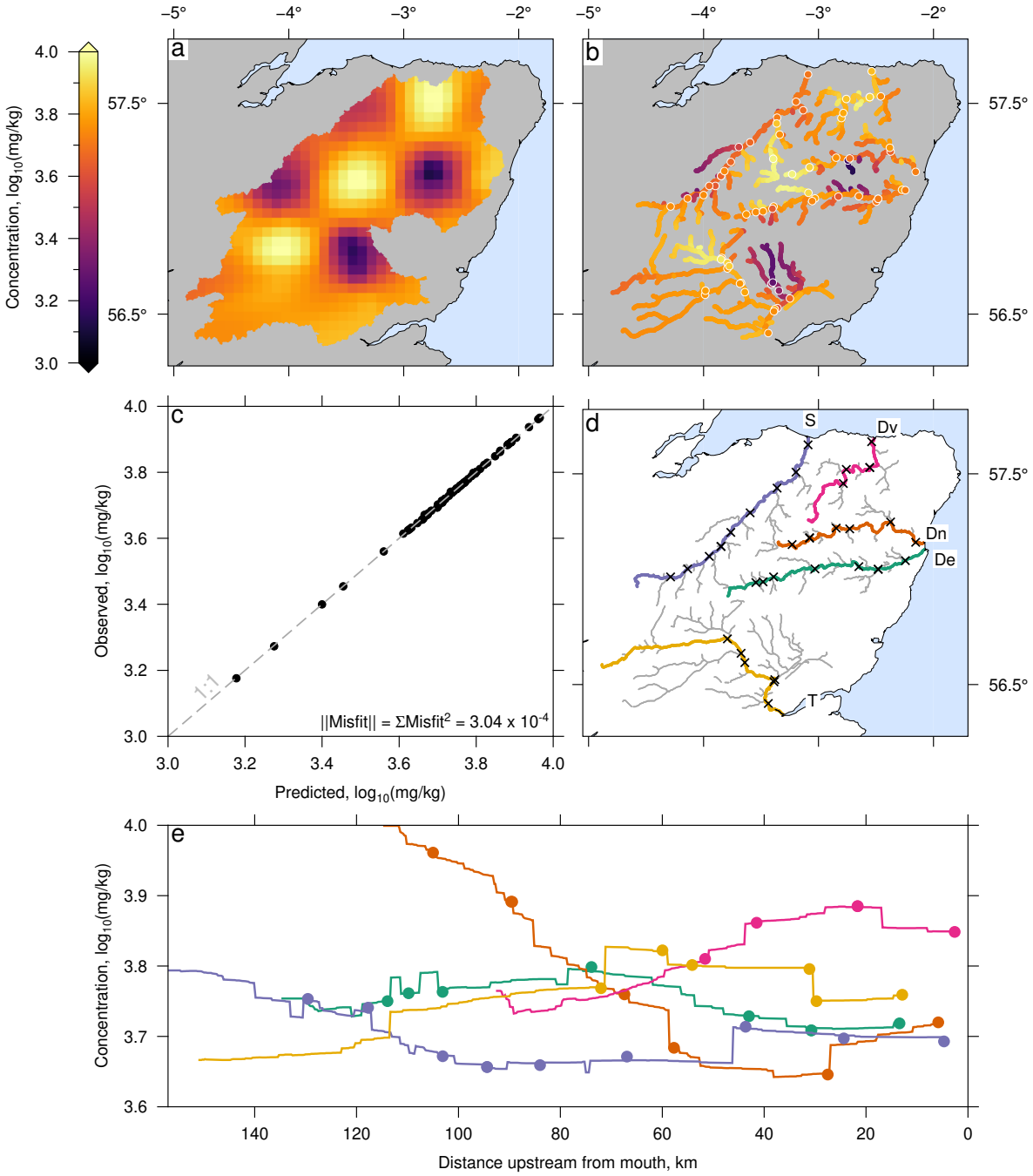

Figure 6: **Downstream chemistry from best fitting inverse model.** (a) Best fitting source region geochemistry generated by inverting synthetic 'samples' shown as coloured circles in panel (b), see Figure 5b. (b) Colored lines = predicted downstream sediment concentrations from best fitting inverse model. Filled circles = synthetic 'observations' that were inverted for source composition. (c) Cross-plot of observed and predicted concentrations at each sample site (black circles). Gray dashed line = 1:1 line. (d) Coloured lines indicate locations of river long-profiles displayed in panel (e): S = Spey, Dv = Deveron, Dn = Don, De = Dee, T = Tay. (e) Coloured lines = predicted sediment concentration from best fitting inverse model along the rivers shown in panels (b) and (d). Colored dots show concentrations at the sample sites indicated by black crosses in panel (d).

the inverse problem and the synthetic input are compared on a cross-plot in Figure 5c. Note that we downsample (i.e., resample onto a lower-resolution grid) the input onto the same resolution as the inverse grid using a block-mean function to allow the two grids to be compared. The data lie clustered close to the 1:1 line with an R^2 of 0.71 and root-mean-square (RMS) misfit of 0.20, indicating that the majority of variance is explained in an unbiased manner by our model.

Plotting the misfit between the synthetic input and the inverse solution spatially indicates where our scheme performs comparatively worse. Figure 5d shows that the residuals are not randomly distributed. This is confirmed by calculating the Moran's I for these residuals, a statistic of autocorrelation which ranges between -1 and +1. Variables with no spatial autocorrelation (i.e., spatially decorrelated) tend to have an $I \sim 0$. We find that the residuals shown in Figure 5d have a Moran's I of 0.08. Whilst this I value is low in magnitiude (indicating a generally small effect size) this value was greater than the expected I under the null hypothesis with a p-value < 0.05 suggesting a statistically significant spatial structure. This structure in the residuals is imparted by spatial changes in sampling density. In the south of the studied region, the residual misfits are larger. This region coincides with low sampling density (Figure 2c; Figure 5b). Where the sample density is more consistently high, across the rest of the region, the signal is successfully recovered.

Figure 6 displays how this best fitting upstream geochemistry relates to the observations of geochemistry downstream. Figure 6b displays the predicted downstream geochemistry for the best-fitting solution displayed in Figure 5b. Overlain on this panel are the synthetic 'observations', which were inverted for upstream composition. Figure 6c is a cross-plot of synthetic 'observed' concentrations against the predicted concentration from the best-fitting inverse model. These points all lie clustered on the 1:1 line indicating that the model was able to fit the downstream data well. The variation in predicted geochemistry of the arbitrary element as a function of downstream distance, with the observations overlain, is shown in Figure 6e. The discrete jumps displayed in the concentration profiles are caused by tributaries joining the main channel. The inverse solution correctly predicts 'observed' downstream variability of sediment geochemistry.

By inputting synthetic signals with patterns of different spatial scales we can qualitatively assess the effective resolution of our scheme. Herein we refer to the different spatial-scales of geochemical features as wavelengths. Figure S-1 displays the inverse results for analogous signals to Figure 5a but with different trough-to-peak distances. When the spatial structure is small ($< O(10)$ km) our scheme cannot resolve any spatial variability. It is however very successful at resolving longer-wavelength spatial structures. These results indicate that, generally, our scheme is able to resolve geochemical spatial structures greater than $\sim 20 - 30$ km.

4.2 Real Data

Having successfully trialled our scheme on synthetic examples we now minimise Equation 5 for the true observed concentration of each of our studied elements independently. The solutions are therefore the best estimate for source region chemistry $C(x, y)$ given the 67 data constraints downstream. These estimates of $C(x, y)$ can be independently tested against the G-BASE geochemical survey dataset. Hence, the veracity of predictions from the inversion scheme can be validated using independent observations.

As an example, we focus first on the results for magnesium. Figure 7a shows the concentration of Mg upstream that best-fits the composition of the 67 downstream samples. Figure 7b shows Mg from the G-BASE database downsampled.to the resolution of the inversion grid. The two maps show the same spatial structure. The low Mg of sediments derived from the felsic intrusions in the centre-left of the region is correctly identified by the inverse solution. Similarly, the two lobes of high-Mg in the upper-right of the region, corresponding to sediments derived from mafic intrusions, are also correctly identified in the best-fitting inverse model. A cross-plot of the inverse solution and G-BASE data is shown in Figure 7c and confirms that our inverse solution correlates with the independent dataset and clusters around the 1:1 line. We emphasise again here that the solution displayed in Figure 7a is completely independent of the G-BASE survey data and calculated using only the 67 data-points we collected downstream.

The predicted downstream geochemistry, i.e., $F(C)$, for this optimal solution is displayed in Figure 8. Comparing the predicted downstream chemistry indicates that the model captures the important geochemical variability within and between drainage basins. However, the model does not overfit the data which, as it likely contains some random noise, is a desirable result. A cross-plot of predicted and observed downstream geochemistry indicates that the model is unbiased with a regression close to the 1:1 line, and explains 76 % of the total variability.

The solutions displayed in Figures 7 and 8 use a smoothing coefficient $\lambda = 10^{0.3}$. This value is chosen as it lies in the 'elbow' of the data-misfit – roughness plot shown in Figure 9a. Each point on this graph corresponds to the roughness and data-misfit of a solution which minimises Equation 5 for a specified λ. Changing the λ affects the extent to which roughness or data-misfit are weighted in Equation 5. The optimum λ value is that which weights both factors without either dominating the total value of the objective functions, resulting in a point which lies in the elbow of the figure. Choosing λ values greater than the optimum clearly over-smooth the solution relative to the independent G-BASE dataset resulting in a poor-fit to the data (Figures 9e-f). Conversely, reducing λ allows the scheme to overfit the data with results which are implausible in reference to the independent dataset (Figures 9b-c). λ must be calibrated in this way for each element.

In Figure 10 we display the optimal solution to the inverse equation against independent data for four other elements, chosen as they show a range of different chemical affinities. Calcium (Figure 10a-b) shows a broadly similar spatial structure to magnesium in both the inverse solution and the independent dataset. The mafic, Ca-rich intrusions in the northeast are correctly identified by the inverse solution as well as the felsic, Ca-poor intrusions in the centre of the region. Rubidium (Figure 10c-d) has a different chemical affinity to Mg and Ca, and is generally associated with felsic rocks. The best-fitting inverse solution for Rb correctly identifies the regions of elevated Rb concentration associated with the felsic-intrusions. Conversely there is a broad region of predicted low-Rb associated with the sedimentary units in the south-east. The distribution of vanadium

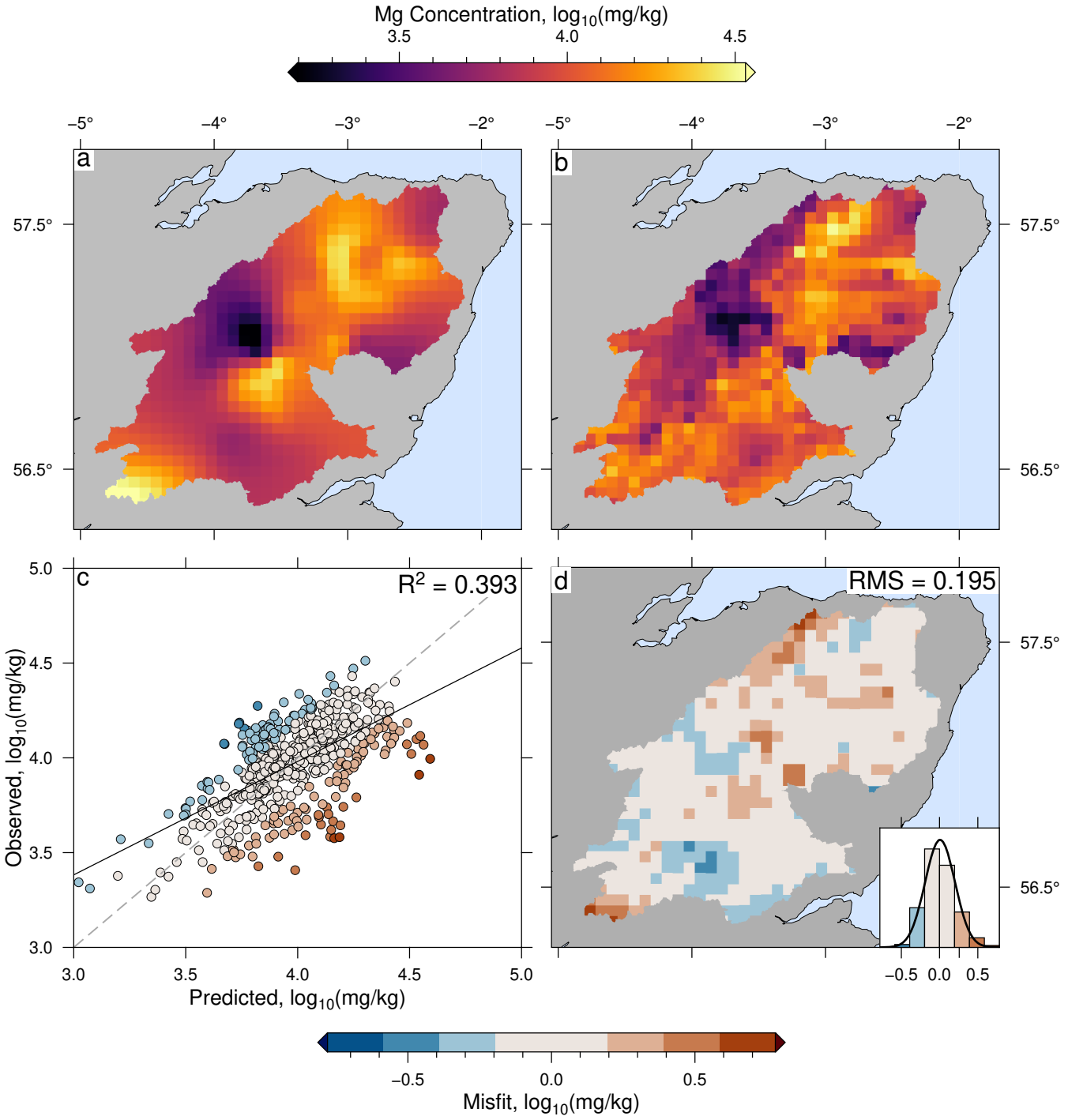

Figure 7: **Inverting real downstream sediment samples for concentration of magnesium in source regions.** (a) Optimum upstream concentration of magnesium generated by inverting the magnesium concentration of the 67 samples gathered downstream with smoothing parameter $\lambda = 10^{0.3}$ (see Figures 4, 8a & body text for details). (b) Independent G-BASE stream sediment concentration of magnesium gridded to same resolution as panel (a); see Figure 3b for full resolution map. (c) Cross-plot of observed (G-BASE) and predicted concentrations for each grid cell (5 km resolution). Colors show misfit discretised at intervals equal to global RMS misfit (0.195). Gray dashed line = 1:1 relationship; black line = linear regression. (d) Misfit between observed magnesium concentration and best-fitting inverse model. Inset indicates distribution of residuals and normal distribution; bin-width = global RMS misfit (0.195). Note higher residuals in regions of low coverage identified in Figure 2c.

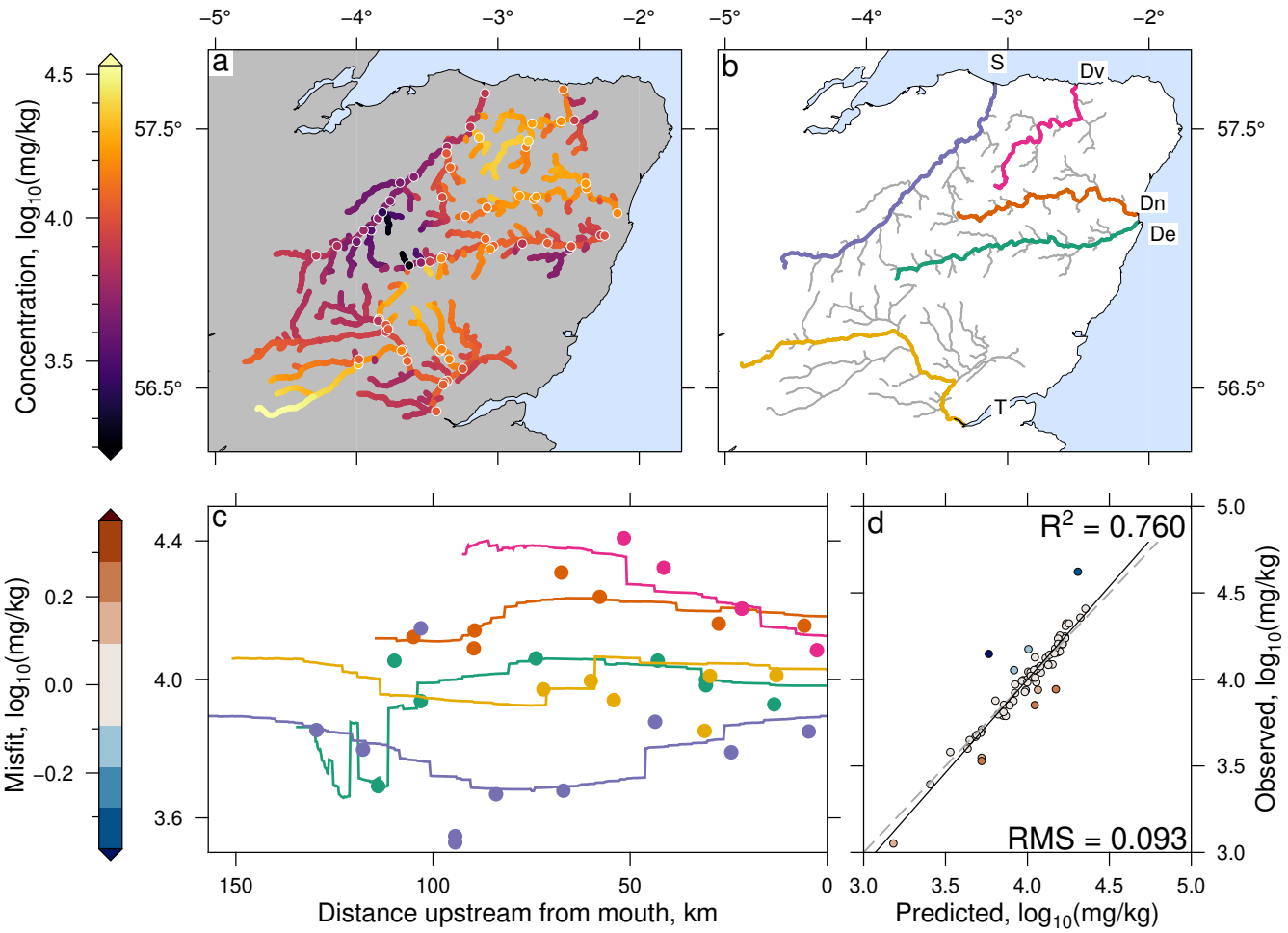

Figure 8: **Evaluating the fit to downstream data from best-fitting inverse model: Magnesium.** (a) Colored circles = measured concentrations at 67 sample sites used to invert for source composition. Colored lines show predicted magnesium sediment concentration along rivers from best-fitting inverse model shown in Figure 7. (b) Colored lines indicate locations of river long-profiles displayed in panel (c): S = Spey, Dv = Deveron, Dn = Don, De = Dee, T = Tay. (c) Colored lines = predicted concentration of magnesium in sediments along rivers shown in panel (b). Colored dots = observed concentrations at the sample-sites shown in panel (a). (d) Cross plot of observed and predicted concentrations of river sediments at the 67 sample sites. Colors = misfit; gray dashed line = 1:1 relationship; black line = regression.

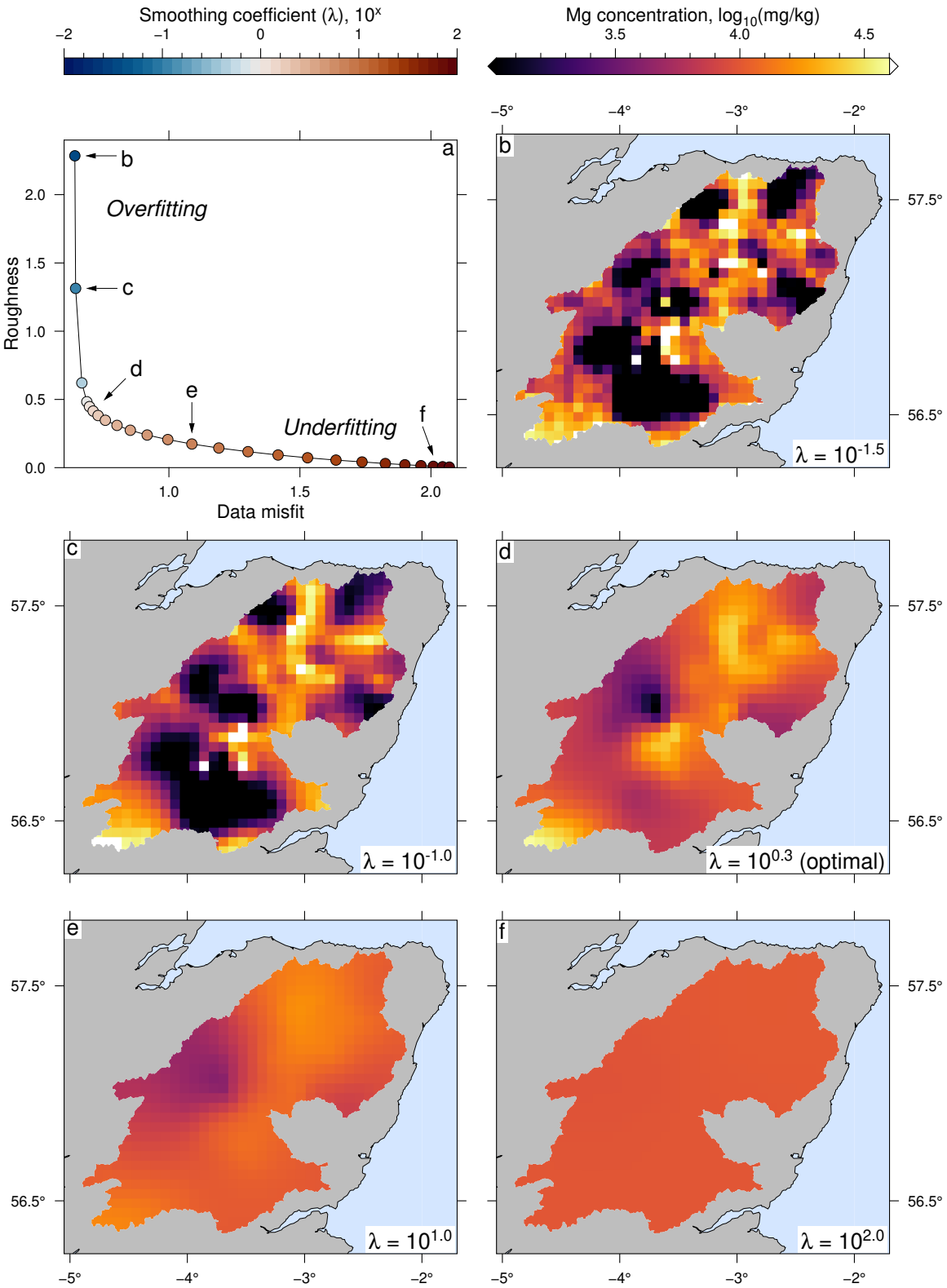

Figure 9: **Identifying the optimum value for smoothing parameter, λ.** (a) Data misfit vs. model roughness for inverse models with different smoothing parameter values (colored circles). This example shows best-fitting concentrations of magnesium. Arrows indicate the points corresponding to the solutions displayed in panels (b–f). Small values of λ result in rough solutions that over-fit the data, e.g., panels (b–c). High values of λ produce smooth solutions that are a poor fit to the data e.g., panels (e–f). Optimum solutions lie in the 'elbow' of this tradeoff plot (Parker 1994). The optimal solution used in this study is shown in panel (d).

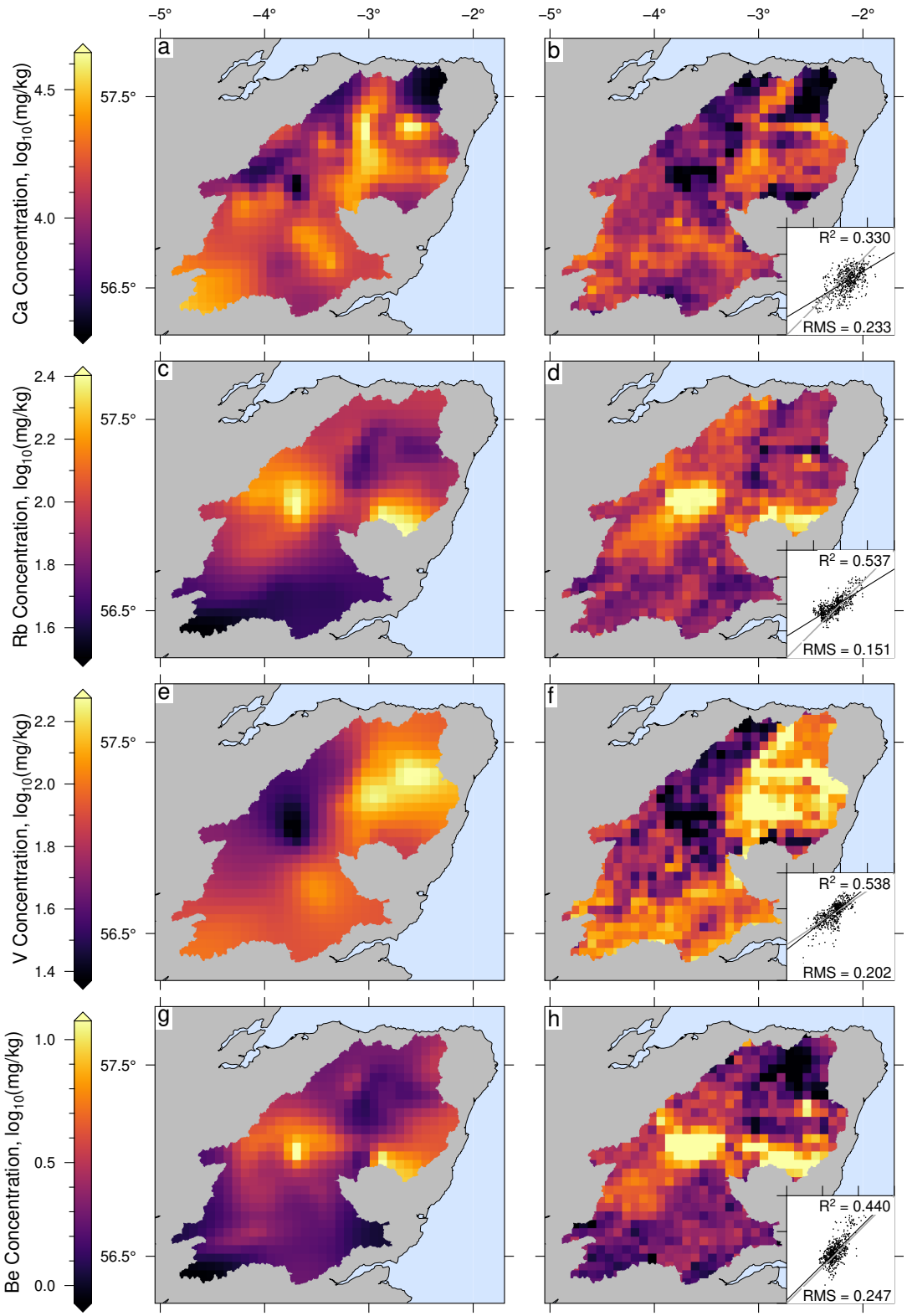

Figure 10: **Inverting selected elements in downstream samples for source composition and a comparison to independent data.** (a) Predicted calcium concentration from inverse model with $\lambda = 10^{-0.3}$. (b) Independent G-BASE stream sediment calcium concentration gridded to same resolution as panel (a). Inset shows cross-plot of observed and best-fitting theoretical concentrations; gray line = 1:1 relationship; black line = regression. (c–d) Rubidium, $\lambda = 10^{0.4}$. (e–f) Vanadium, $\lambda = 10^{0.7}$. (g–h) Beryllium, $\lambda = 10^{0.3}$.

is different again to the previous elements, and appears to be mostly set by NE-SW trending distribution of sedimentary units. These separate domains are correctly identified by the inverse solution. Beryllium has a similar spatial structure to rubidium, consistent with its association with felsic units. The best fitting maps for all other studied elements are given in the Supporting Information (Figures S-2 to S-22).

These results indicate that the inversion is able to successfully recover the spatial distribution of geochemistry for elements with a range of different geochemical affinities. We can formally assess the similarities between our inverse solutions and the G-BASE dataset using the R^2 and RMS. These values for all elements are shown in Figure 11. Figure 11a shows the statistics comparing our upstream predictions against the independent G-BASE dataset. Figure 11b compares the predicted and observed concentrations for the downstream sediment concentration. Note that results are not presented for Cu and Pb as not enough solutions at different λ values were able to be found to reliably choose an optimum value. Inverse models failed to converge on a solution in a reasonable amount of time for these elements given our tolerance and smoothing values. The mean R^2 for the upstream predictions against the independent G-BASE dataset is 0.322, with an RMS of 0.226. For fitting the downstream data we have a mean R^2 and RMS of 0.776 and 0.0863, respectively.

4.3 Multivariate analysis

Studying the results from inverse modelling of individual element neglects the important relationships that exist between elements. If our inverse scheme is successful it should also be able to recover geologically plausible relationships between different elements. By applying PCA to the upstream inverse solutions for all of our studied elements we can see if our inversion has captured meaningful associations between the different elements. In addition, by plotting these associations spatially we can see if it has recovered the different geochemical domains for the region identified in Figure 3.

The first three PCs of our suite of inverse results are shown in Figure 12a using a RGB ternary space. The relationships between the geochemical elements and these PCs are shown in Figure 12d. The first PC corresponds to relative enrichment in felsic lithophile elements (e.g., U, Be). The second PC is associated with metals (e.g., Ni, Co, Ti) and the third appears to be associated with mafic lithophile elements (Mg, Ca). These associations are very similar to the principal geochemical relationships of the G-BASE dataset (Figure 3e-f). This result indicates that our inverse solution has correctly identified the major geochemical associations of this region. Moreover, the spatial distribution of these associations mimics that of the G-BASE PCA map, albeit with finer resolution details unresolvable. The similarities of the G-BASE data structure to that of our inverse solution, and their similar spatial pattern, indicates that the inverse procedure has successfully recovered the principal geochemical variability of the region.

5 DISCUSSION

5.1 Sediment geochemistry as deterministic

Our inverse scheme is able to produce maps of upstream geochemistry that are validated against independent data and capture the dominant long-wavelength geochemical features of a large area. Successful unmixing suggests that sedimentary geochemistry is a largely deterministic process dominated by mixing. Deterministic behaviour is strongly encouraging for attempts to build quantitative models of sediment provenance, an approach termed 'quantitative provenance analysis' (Weltje and Eynatten 2004). Moreover our results validate approaches that have previously attempted to describe sediment geochemistry assuming conservative behaviour (e.g. Garzanti et al. 2012; Ercolani et al. 2019). Significantly, our predictions are unbiased against independent data with residuals generally distributed normally around zero. This result suggests that geochemical modification of sediments in transit through our studied drainage networks is negligible. Whilst we consider the inorganic sediment fraction only in this study, this approach could in principle be used to understand organic geochemistry which is also strongly controlled by mixing (Menges et al. 2020).

The success of our model, which does not explicitly consider climatic effects, may be considered surprising given other studies which demonstrate that climatic factors, via chemical weathering are a significant control on fluvial sedimentary geochemistry (e.g., Canfield 1997; Riebe et al. 2003; Garzanti et al. 2013, 2014; Dinis et al. 2017). However, the results are not inconsistent. Our results imply that weathering of sediment takes place in-situ before sediment enters the fluvial system. Therefore, any relationship between climate and weathering occurs before fluvial transport, i.e. on hillslopes. That our predicted source-region geochemistry appears to be controlled almost entirely by lithology (and hence not climate) is because we only consider relatively small catchments which do not cross any significant climatic gradients. By contrast, an analogous study in areas of strong climatic gradients (e.g., Angola; Dinis et al. 2017) may produce maps of source region geochemistry with a correlation to climate, with lithology taking a secondary role. We note that globally there is, however, only a weak observed relationship between the composition of large river sediments and the climatic parameters of river basins (Gaillardet et al. 1999). This result could be explained by the fact that the potential obscuring effects of intra-catchment mixing have not been sufficiently accounted for prior to comparison to climate parameters. An unmixing approach similar to the one we propose could therefore be used to correct for mixing effects better revealing the role of climate.

5.2 Non-conservative behaviour

An exception to the general rule of unbiased predictions (i.e., residuals distributed around zero) appears to be calcium, which our inversion scheme tends to over-predict relative to G-BASE upstream (Figure 10a-b; Figure S-5). One possible explanation for this could be the adsorption of dissolved calcium cations to the surface of clays in sediments, a process that is observed in rivers globally (Sayles and Mangelsdorf 1979; Lupker et al. 2016; Tipper et al. 2021).

Zirconium, in contrast to Ca, is underpredicted in our inverse solutions (Figure S-22). This is caused by the fact that our method of chemical analysis can underpredict elements hosted in resistate minerals, as discussed in the Methods section. As a result, the predictions upstream inherit this underprediction. Notably however, the predicted spatial structure of Zr is similar to that of the independent dataset, but offset to lower values. The

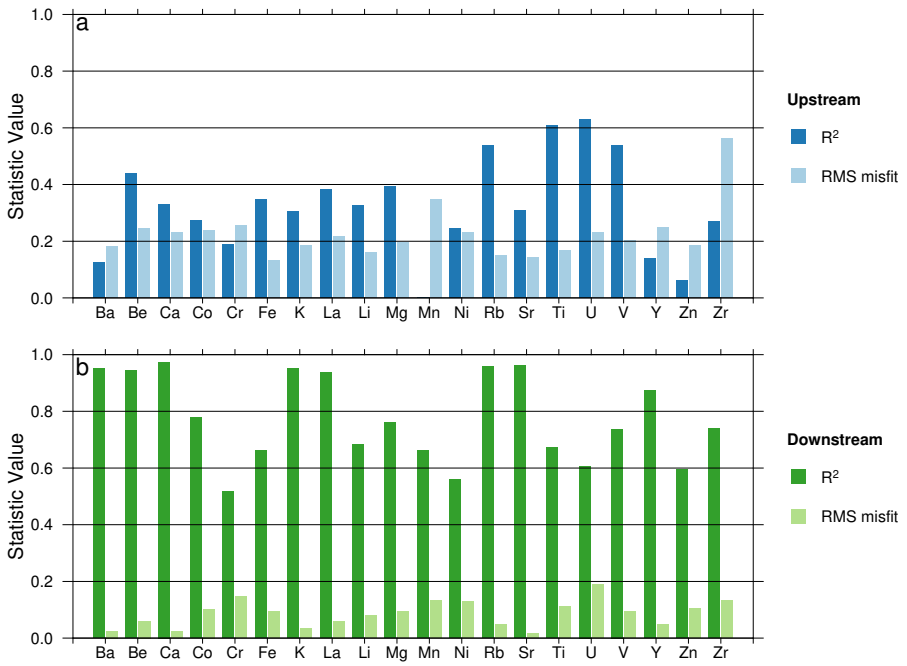

Figure 11: **Statistical evaluation of inverse solutions.** (a) R^2 values and RMS misfit for best-fitting theoretical upstream geochemistry relative to independent G-BASE dataset. See Figures 8 and 10 for visualisation of this comparison. (b) R^2 values and RMS misfit of predicted downstream concentration relative to the 67 samples inverted for upstream composition. See Figure 8 for a visualisation of this comparison

successful recovery of spatial structure, despite a propagated analytical error, indicates the robustness of our scheme to data and that errors in the data propagate predictably through our scheme.

5.3 Resolution

The spatial pattern of misfit in both synthetic and real examples (Figures 5 and 7) indicates that low sample density in the south of our studied region is at present the most significant source of uncertainty. In future this could be readily resolved by designing sample campaigns with the specific goal of creating nested-catchments with equal area, so that coverage is equal across the studied region.

Ultimately, the effective resolution of our scheme is equal to the areas of the nested subcatchments shown in Figure 2c. Any spatial variability within a sub-catchment is averaged out and hence unresolvable. As a result we can consider our inversion scheme to be producing a low-pass filtered (i.e., small spatial structures removed) version of the true source region geochemical map. This is confirmed by directly comparing our inversion results against the G-BASE survey data when both have undergone low-pass filtering as shown in Figure 13. This figure shows the maps produced by our scheme, and G-BASE, after being smoothed using a 2D Gaussian filter of width 25 km, the estimated effective-resolution of our scheme as deduced from synthetic inversions (see Figure S-1). The spatial structure of the two filtered maps is extremely similar for all four displayed elements. Hence our scheme can be considered as generating low-pass filtered geochemical maps, with a wavelength set by the sampling density. The effective resolution of the inverse model can therefore be increased with higher sampling densities. A theoretically infinitely dense campaign where every part of the drainage network was sampled would be able to recover the full spatial signal (neglecting the influence of stochastic noise). The shape of

5.4 Limitations

There is some variability in the R^2 values between different elements. Notably, our inverse result for Mn has an R^2 close to zero, indicating that our estimates show no relationship to the upstream geochemistry. However, this result should be considered against the fact that the Mn G-BASE data (and other elements with low R^2) shows very limited long-wavelength spatial structure (Figure S-13) with most of the variability dominated by short-wavelength 'noise'. As a result, part of the reason our scheme fails to replicate the independent data in the case of Mn is that there is very limited long-wavelength spatial structure to resolve in the first instance. Our scheme, which acts as a low-pass filter (see above) hence has low R^2 values for elements whose variability is dominantly set on short-wavelengths. This limitation can hence be readily remedied by greater sampling densities, if it were necessary for any reason to recover the spatial structure of these elements dominantly set on short-wavelengths.

This behaviour is partially a limitation of the R^2 as a measure of success in that for signals where there is a low signal to noise ratio, the R^2 will always remain low. The alternative measure of success we use is the RMS misfit relative to the independent G-BASE dataset. This value shows more consistency between elements (Figure 11) and can be considered analogous to the 1

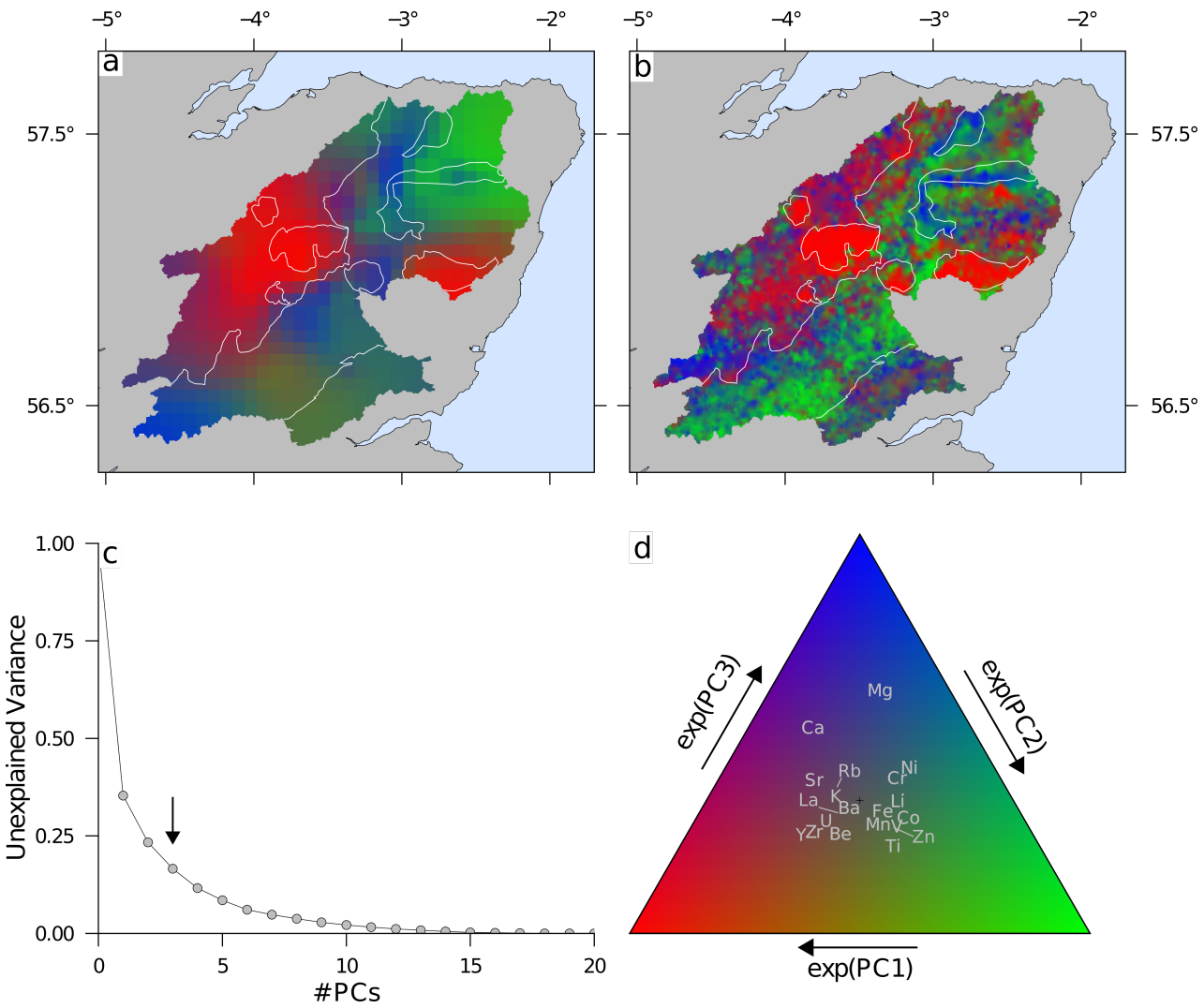

Figure 12: **Mapping geochemical domains using multivariate analysis and inverse modelling.** (a) Principal component (PC) map generated using best-fitting inverse models for the 20 elements shown in Figure 11. The first three PCs were extracted from the best-fitting inverse models and passed into a red-green-blue (RGB) ternary space. See panel (d) for key. Note strong similarity to the principal component map generated from the G-BASE dataset displayed in Figure 3e and the relationship to lithological boundaries (white lines). (c) Variance explained for each principal component. Arrow indicates chosen number of PCs (3) which explain 83 % of the total variability. (d) RGB ternary plot. Reds indicate enrichment in elements with felsic association (e.g., U, Be). Greens indicate enrichment in metallic association elements (e.g., Ni, Co, Ti). Blues indicate mafic association elements (e.g., Mg, Ca).

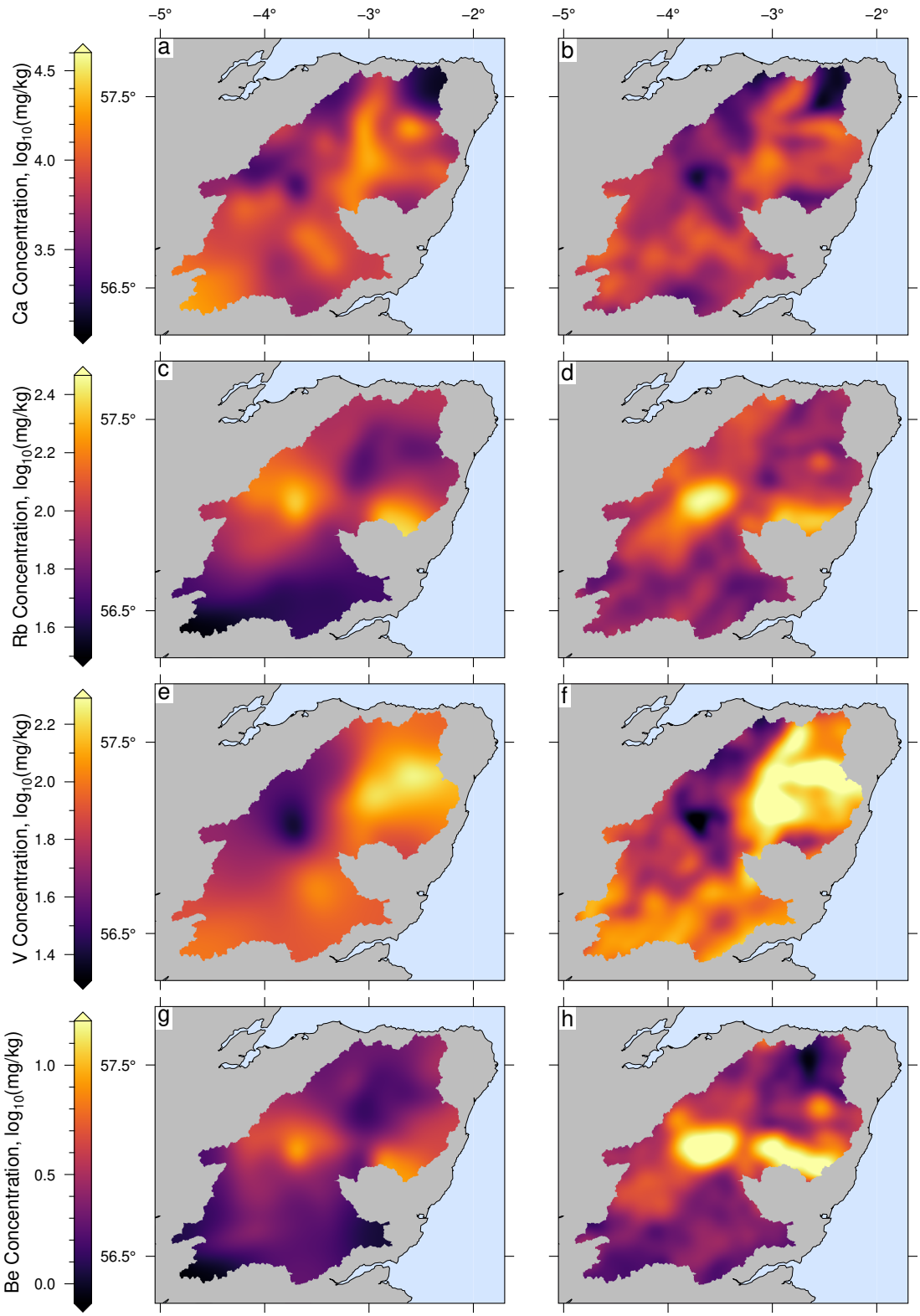

Figure 13: **Comparison of long wavelength (> 25 km) components of predicted and observed source region geochemistry.** (a) Low-pass filter of predicted calcium concentrations. Figure 10a was filtered using a 2D Gaussian filter of width 25 km. (b) Ca concentrations from the G-BASE dataset low-pass filtered using the same Gaussian filter. (c–d) Rubidium. (e–f) Vanadium. (g–h) Beryllium. Note that a comparison between the long wavelength components of observed and predicted magnesium concentrations are given in Supporting Information.

σ uncertainty of our predictions. Hence, our predictions have a relative uncertainty of 0.226, i.e., $x \times 10^{\pm 0.226}$. These confidence intervals are well within an order of magnitude and testify to the general success of our model in mapping regional geochemistry for a range of different elements.

5.5 *Mapping geochemical baselines using inverse modelling*

Producing geochemical maps of Earth's surface remains an ongoing challenge for applied geochemistry. Geochemical maps are essential data-products for identifying regions of elevated elemental concentrations which may indicate economic mineralisation or contamination. Further, such maps may impact on the application of regulatory controls or agricultural land management (Ander et al. 2013). However, it is estimated that at present only $\sim$ 20 % of the Earth's surface has been mapped geochemically at any scale (Liu et al. 2021). Part of this challenge is due to the fact that mapping large, continental-scale, areas is logistically challenging and can be extremely expensive due to the large numbers of geochemical samples that must be processed. As a result, considerable attention has been focussed on developing methods to produce geochemical maps with small numbers of samples (e.g., Smith and Reimann 2008; Cicchella et al. 2013; Birke et al. 2015; Liu et al. 2021).

In our studied region, an area of 12,800 km^2, the G-BASE survey collected $\sim$ 8,000 samples corresponding to a sampling density of 1 *per* 1.7 km^2. By contrast, in our scheme we utilise only 67 samples, resulting in a density of 1 *per* 192 km^2. Despite this much lower sample density our inverse procedure was still able to identify the dominant spatial geochemical structures of the region. Whilst our scheme cannot resolve the very fine spatial structures in many instances this limitation may be reasonable given the significant reduction in samples required. Hence, unmixing of higher-order stream sediments could be a powerful new way to geochemically map large areas at low sample densities.

6 Conclusions

We have presented a novel inverse procedure to unmix the composition of river-sediments to produce geochemical maps of source regions. This scheme is tested using real data gathered from five rivers in the Cairngorms, UK. Testing this scheme using synthetic input data indicates it can recover upstream spatial signals at scales > 20 km. Using 67 downstream sediment samples we have mapped the elemental concentration of 20 elements across an area of 12,800 km^2. These predicted maps are validated against independent geochemical data gathered from geochemical surveying. Our predictions are found to be generally unbiased and successfully recover the long-wavelength (> 20 km) spatial structure of the region. Our procedure also successfully identifies meaningful geochemical associations between different elements as revealed by multivariate analysis. The success of this unmixing procedure indicates that in-transit modification of bulk sediment geochemistry is subordinate to the the effect of mixing. Such inverse approaches are a novel way to map the geochemistry of large areas at a low sampling density. Our results indicates that sedimentary elemental geochemistry is in part deterministic. Our approach is a step towards fully quantitative models of sediment provenance.

Data and Code Availability

Code and data is available at github.com/AlexLipp/unmixer and archived at the point of submission at doi.org/10.5281/zenodo.4693005.

Author Contributions

AGL, GGR and ACW conceived of the study; AGL, ACW, GGR and VMF performed sample collection; AGL and CJBG performed sample preparation and geochemical analysis in the Inorganic geochemistry Laboratories at the BGS; AGL performed data analysis and code development; AGL and GGR wrote the manuscript; all authors contributed to manuscript revision.

Acknowledgements

This research was improved by helpful discussions with C. O'Malley, E. L. Ander and T. R. Lister. This research was supported by CASP. AGL is funded by the Natural Environment Research Council Grantham Institute SSCP DTP [grant number NE/L002515/1] and performed labwork at BGS under a BUFI studentship.

References

Aitchison, J. (1983). "Principal component analysis of compositional data". *Biometrika* 70.1, pp. 57–65. DOI: 10.1093/biomet/70.1.57.

Aitchison, J. (1986). *The statistical analysis of compositional data*. Chapman and Hall.

Ander, E. L., C. C. Johnson, M. R. Cave, B. Palumbo-Roe, C. P. Nathanail, and R. M. Lark (2013). "Methodology for the determination of normal background concentrations of contaminants in English soil". *Science of The Total Environment* 454-455, pp. 604–618. DOI: 10.1016/j.scitotenv.2013.03.005.

Barnes, R., C. Lehman, and D. Mulla (2014). "Priority-flood: An optimal depression-filling and watershed-labeling algorithm for digital elevation models". *Computers & Geosciences* 62, pp. 117–127. DOI: 10.1016/j.cageo.2013.04.024.

Barnhart, K. R., E. W. H. Hutton, G. E. Tucker, N. M. Gasparini, E. Istanbulluoglu, D. E. J. Hobley, N. J. Lyons, M. Mouchene, S. S. Nudurupati, J. M. Adams, and C. Bandaragoda (2020). "Short communication: Landlab v2.0: a software package for Earth surface dynamics". *Earth Surface Dynamics* 8.2, pp. 379–397. DOI: https://doi.org/10.5194/esurf-8-379-2020.

Birke, M., U. Rauch, and J. Stummeyer (2015). "How robust are geochemical patterns? A comparison of low and high sample density geochemical mapping in Germany". *Journal of Geochemical Exploration* 154, pp. 105–128. DOI: 10.1016/j.gexplo.2014.12.005.

Bouchez, J., J. Gaillardet, C. France-Lanord, L. Maurice, and P. Dutra-Maia (2011). "Grain size control of river suspended sediment geochemistry: Clues from Amazon River depth profiles". *Geochemistry, Geophysics, Geosystems* 12.3. DOI: 10.1029/2010GC003380.

Bouchez, J., J. Gaillardet, M. Lupker, P. Louvat, C. France-Lanord, L. Maurice, E. Armijos, and J.-S. Moquet (2012). "Floodplains of large rivers: Weathering reactors or simple silos?" *Chemical Geology* 332-333, pp. 166–184. DOI: 10.1016/j.chemgeo.2012.09.032.

Canfield, D. E. (1997). "The geochemistry of river particulates from the continental USA: major elements". *Geochimica Et Cosmochimica Acta* 61.16, pp. 3349–3365.

Caracciolo, L. (2020). "Sediment generation and sediment routing systems from a quantitative provenance analysis perspective: Review, application and future development". *Earth-Science Reviews* 209, p. 103226. DOI: 10.1016/j.earscirev.2020.103226.

Caritat, P. d. and M. Cooper (2016). "A continental-scale geochemical atlas for resource exploration and environmental management: the National Geochemical Survey of Australia". *Geochemistry: Exploration, Environment, Analysis* 16.1, pp. 3–13. DOI: 10.1144/geochem2014-322.

Cicchella, D., A. Lima, M. Birke, A. Demetriades, X. Wang, and B. De Vivo (2013). "Mapping geochemical patterns at regional to continental scales using composite samples to reduce the analytical costs". *Journal of Geochemical Exploration* 124, pp. 79–91. DOI: 10.1016/j.gexplo.2012.08.012.

Dam, J. A. van and G. J. Weltje (1999). "Reconstruction of the Late Miocene climate of Spain using rodent palaeocommunity successions: an application of end-member modelling". *Palaeogeography, Palaeoclimatology, Palaeoecology* 151.4, pp. 267–305. DOI: 10.1016/S0031-0182(99)00015-2.

De Doncker, F., F. Herman, and M. Fox (2020). "Inversion of provenance data and sediment load into spatially varying erosion rates". *Earth Surface Processes and Landforms* 45.15, pp. 3879–3901. DOI: https://doi.org/10.1002/esp.5008.

Dekkers, M. J. (2012). "End-member modelling as an aid to diagnose remagnetization: a brief review". *Geological Society, London, Special Publications* 371.1, pp. 253–269. DOI: 10.1144/SP371.12.

Dinis, P., E. Garzanti, P. Vermeesch, and J. Huvi (2017). "Climatic zonation and weathering control on sediment composition (Angola)". *Chemical Geology* 467, pp. 110–121. DOI: 10.1016/j.chemgeo.2017.07.030.

Ercolani, C., D. Lemarchand, and A. Dosseto (2019). "Insights on catchment-wide weathering regimes from boron isotopes in riverine material". *Geochimica et Cosmochimica Acta*. DOI: 10.1016/j.gca.2019.07.002.

Everett, P., A. Donald, A. Ferreira, F. Fordyce, C. Gowing, R. Lawley, T. Lister, B. Palumbo-Roe, and British Geological Survey (2019). *Stream sediment geochemical atlas of the United Kingdom: British Geological Survey report OR/18/048*. British Geological Survey.

Farr, T. G., P. A. Rosen, E. Caro, R. Crippen, R. Duren, S. Hensley, M. Kobrick, M. Paller, E. Rodriguez, L. Roth, D. Seal, S. Shaffer, J. Shimada, J. Umland, M. Werner, M. Oskin, D. Burbank, and D. Alsdorf (2007). "The Shuttle Radar Topography Mission". *Reviews of Geophysics* 45.2. DOI: 10.1029/2005RG000183.

Gaillardet, J., B. Dupré, and C. J. Allègre (1999). "Geochemistry of large river suspended sediments: silicate weathering or recycling tracer?" *Geochimica et Cosmochimica Acta* 63.23, pp. 4037–4051. DOI: 10.1016/S0016-7037(99)00307-5.

Gao, F. and L. Han (2012). "Implementing the Nelder-Mead simplex algorithm with adaptive parameters". *Computational Optimization and Applications* 51.1, pp. 259–277. DOI: 10.1007/s10589-010-9329-3.

Garrett, R., C. Reimann, D. Smith, and X. Xie (2008). "From geochemical prospecting to international geochemical mapping: a historical overview". *Geochemistry: Exploration, Environment, Analysis* 8.3, pp. 205–217. DOI: 10.1144/1467-7873/08-174.

Garzanti, E., M. Padoan, M. Setti, A. López-Galindo, and I. M. Villa (2014). "Provenance versus weathering control on the composition of tropical river mud (southern Africa)". *Chemical Geology* 366, pp. 61–74. DOI: 10.1016/j.chemgeo.2013.12.016.

Garzanti, E., M. Padoan, M. Setti, Y. Najman, L. Peruta, and I. M. Villa (2013). "Weathering geochemistry and Sr-Nd fingerprints of equatorial upper Nile and Congo muds". *Geochemistry, Geophysics, Geosystems* 14.2, pp. 292–316. DOI: 10.1002/ggge.20060.

Garzanti, E., A. Resentini, G. Vezzoli, S. Andò, M. Malusà, and M. Padoan (2012). "Forward compositional modelling of Alpine orogenic sediments". *Sedimentary Geology*. Actualistic Models of Sediment Generation 280, pp. 149–164. DOI: 10.1016/j.sedgeo.2012.03.012.

Howard, A. D. and G. Kerby (1983). "Channel changes in badlands". *GSA Bulletin* 94.6, pp. 739–752. DOI: 10.1130/0016-7606(1983)94<739:CCIB>2.0.CO;2.

Johnson, C. C., N. Breward, E. L. Ander, and L. Ault (2005). "G-BASE: baseline geochemical mapping of Great Britain and Northern Ireland". *Geochemistry: Exploration, Environment, Analysis* 5.4, pp. 347–357. DOI: 10.1144/1467-7873/05-070.

Johnson, C. C., E. L. Ander, T. R. Lister, and D. M. A. Flight (2018a). "Data Conditioning of Environmental Geochemical Data: Quality Control Procedures Used in the British Geological Survey's Regional Geochemical Mapping Project". In: *Environmental Geochemistry (Second Edition)*. Ed. by B. De Vivo, H. E. Belkin, and A. Lima. 2nd ed. Elsevier, pp. 79–101. DOI: 10.1016/B978-0-444-63763-5.00006-9.

Johnson, C. C., D. M. A. Flight, E. L. Ander, T. R. Lister, N. Breward, F. M. Fordyce, S. E. Nice, and K. V. Knights (2018b). "The Collection of Drainage Samples for Environmental Analyses From Active Stream Channels". In: *Environmental Geochemistry (Second Edition)*. Ed. by B. De Vivo, H. E. Belkin, and A. Lima. Elsevier, pp. 47–77. DOI: 10.1016/B978-0-444-63763-5.00005-7.

Kirkwood, C., P. Everett, A. Ferreira, and B. Lister (2016). "Stream sediment geochemistry as a tool for enhancing geological understanding: An overview of new data from south west England". *Journal of Geochemical Exploration* 163, pp. 28–40. DOI: 10.1016/j.gexplo.2016.01.010.

Lipp, A. G., G. G. Roberts, A. C. Whittaker, C. J. B. Gowing, and V. M. Fernandes (2020). "River Sediment Geochemistry as a Conservative Mixture of Source Regions: Observations and Predictions From the Cairngorms, UK". *Journal of Geophysical Research: Earth Surface* 125.12, e2020JF005700. DOI: https://doi.org/10.1029/2020JF005700.

Liu, D., X. Wang, L. Nie, H. Liu, B. Zhang, and W. Wang (2021). "Comparison of geochemical patterns from different sampling density geochemical mapping in Altay, Xinjiang Province, China". *Journal of Geochemical Exploration*, p. 106761. DOI: 10.1016/j.gexplo.2021.106761.

Lupker, M., C. France-Lanord, V. Galy, J. Lavé, J. Gaillardet, A. P. Gajurel, C. Guilmette, M. Rahman, S. K. Singh, and R. Sinha (2012). "Predominant floodplain over mountain weathering of Himalayan sediments (Ganga basin)". *Geochimica et*

Cosmochimica Acta 84, pp. 410–432. DOI: 10.1016/j.gca.2012.02.001.

Lupker, M., C. France-Lanord, V. Galy, J. Lavé, and H. Kudrass (2013). "Increasing chemical weathering in the Himalayan system since the Last Glacial Maximum". *Earth and Planetary Science Letters* 365, pp. 243–252. DOI: 10.1016/j.epsl.2013.01.038.

Lupker, M., C. France-Lanord, and B. Lartiges (2016). "Impact of sediment–seawater cation exchange on Himalayan chemical weathering fluxes". *Earth Surface Dynamics* 4.3, pp. 675–684. DOI: https://doi.org/10.5194/esurf-4-675-2016.

Menges, J., N. Hovius, C. Andermann, M. Lupker, N. Haghipour, L. Märki, and D. Sachse (2020). "Variations in organic carbon sourcing along a trans-Himalayan river determined by a Bayesian mixing approach". *Geochimica et Cosmochimica Acta* 286, pp. 159–176. DOI: 10.1016/j.gca.2020.07.003.

O'Callaghan, J. F. and D. M. Mark (1984). "The extraction of drainage networks from digital elevation data". *Computer Vision, Graphics, and Image Processing* 28.3, pp. 323–344. DOI: 10.1016/S0734-189X(84)80011-0.

Parker, R. L. (1994). *Geophysical Inverse Theory*. Vol. 1. Princeton University Press. DOI: 10.2307/j.ctvs32s89.

Pawlowsky-Glahn, V. and J. J. Egozcue (2006). "Compositional data and their analysis: an introduction". *Geological Society, London, Special Publications* 264.1, pp. 1–10.

Pedregosa, F., G. Varoquaux, A. Gramfort, V. Michel, B. Thirion, O. Grisel, M. Blondel, P. Prettenhofer, R. Weiss, V. Dubourg, J. Vanderplas, A. Passos, D. Cournapeau, M. Brucher, M. Perrot, and É. Duchesnay (2011). "Scikit-learn: Machine Learning in Python". *Journal of Machine Learning Research* 12.85, pp. 2825–2830.

Press, W. H., S. A. Teukolsky, W. T. Vetterling, and B. P. Flannery (1992). *Numerical Recipes in FORTRAN: The Art of Scientific Computing*. 2nd ed. New York, NY: Cambridge University Press.

Repasch, M., H. Wittmann, J. S. Scheingross, D. Sachse, R. Szupiany, O. Orfeo, M. Fuchs, and N. Hovius (2020). "Sediment Transit Time and Floodplain Storage Dynamics in Alluvial Rivers Revealed by Meteoric 10Be". *Journal of Geophysical Research: Earth Surface* 125.7, e2019JF005419. DOI: 10.1029/2019JF005419.

Riebe, C. S., J. W. Kirchner, and R. C. Finkel (2003). "Long-term rates of chemical weathering and physical erosion from cosmogenic nuclides and geochemical mass balance". *Geochimica et Cosmochimica Acta* 67.22, pp. 4411–4427. DOI: 10.1016/S0016-7037(03)00382-X.

Sayles, F. L. and P. C. Mangelsdorf (1979). "Cation-exchange characteristics of Amazon River suspended sediment and its reaction with seawater". *Geochimica et Cosmochimica Acta* 43.5, pp. 767–779. DOI: 10.1016/0016-7037(79)90260-6.

Schneider, S., J. Hornung, M. Hinderer, and E. Garzanti (2016). "Petrography and geochemistry of modern river sediments in an equatorial environment (Rwenzori Mountains and Albertine rift, Uganda) — Implications for weathering and provenance". *Sedimentary Geology*. Sediment generation and provenance: processes and pathways 336, pp. 106–119. DOI: 10.1016/j.sedgeo.2016.02.006.

Sharman, G. R., Z. Sylvester, and J. A. Covault (2019). "Conversion of tectonic and climatic forcings into records of sediment supply and provenance". *Scientific Reports* 9.1, p. 4115. DOI: 10.1038/s41598-019-39754-6.

Smith, D. B. and C. Reimann (2008). "Low-density geochemical mapping and the robustness of geochemical patterns". *Geochemistry: Exploration, Environment, Analysis* 8.3, pp. 219–227. DOI: 10.1144/1467-7873/08-171.

Stock, B. C., A. L. Jackson, E. J. Ward, A. C. Parnell, D. L. Phillips, and B. X. Semmens (2018). "Analyzing mixing systems using a new generation of Bayesian tracer mixing models". *PeerJ* 6, e5096. DOI: 10.7717/peerj.5096.

Tipper, E. T., E. I. Stevenson, V. Alcock, A. C. G. Knight, J. J. Baronas, R. G. Hilton, M. J. Bickle, C. S. Larkin, L. Feng, K. E. Relph, and G. Hughes (2021). "Global silicate weathering flux overestimated because of sediment–water cation exchange". *Proceedings of the National Academy of Sciences* 118.1, e2016430118. DOI: 10.1073/pnas.2016430118.

Tucker, G. E. and K. X. Whipple (2002). "Topographic outcomes predicted by stream erosion models: Sensitivity analysis and intermodel comparison". *Journal of Geophysical Research: Solid Earth* 107 (B9), ETG 1–1–ETG 1–16. DOI: 10.1029/2001JB000162.

Van Rossum, G. and F. L. Drake (2009). *Python 3 Reference Manual*. Scotts Valley, CA: CreateSpace.

Viers, J., B. Dupré, and J. Gaillardet (2009). "Chemical composition of suspended sediments in World Rivers: New insights from a new database". *Science of The Total Environment* 407.2, pp. 853–868. DOI: 10.1016/j.scitotenv.2008.09.053.

Virtanen, P., R. Gommers, T. E. Oliphant, M. Haberland, T. Reddy, D. Cournapeau, E. Burovski, P. Peterson, W. Weckesser, J. Bright, S. J. van der Walt, M. Brett, J. Wilson, K. J. Millman, N. Mayorov, A. R. J. Nelson, E. Jones, R. Kern, E. Larson, C. J. Carey, İ. Polat, Y. Feng, E. W. Moore, J. VanderPlas, D. Laxalde, J. Perktold, R. Cimrman, I. Henriksen, E. A. Quintero, C. R. Harris, A. M. Archibald, A. H. Ribeiro, F. Pedregosa, and P. van Mulbregt (2020). "SciPy 1.0: fundamental algorithms for scientific computing in Python". *Nature Methods* 17.3, pp. 261–272. DOI: 10.1038/s41592-019-0686-2.

Weltje, G. J. (1997). "End-member modeling of compositional data: Numerical-statistical algorithms for solving the explicit mixing problem". *Mathematical Geology* 29.4, pp. 503–549. DOI: 10.1007/BF02775085.

– (2012). "Quantitative models of sediment generation and provenance: State of the art and future developments". *Sedimentary Geology*. Actualistic Models of Sediment Generation 280, pp. 4–20. DOI: 10.1016/j.sedgeo.2012.03.010.

Weltje, G. J. and H. von Eynatten (2004). "Quantitative provenance analysis of sediments: review and outlook". *Sedimentary Geology*. Quantitative Provenance Analysis of Sediments 171.1, pp. 1–11. DOI: 10.1016/j.sedgeo.2004.05.007.

Weltje, G. J. and M. A. Prins (2007). "Genetically meaningful decomposition of grain-size distributions". *Sedimentary Geology*. From Particle Size to Sediment Dynamics 202.3, pp. 409–424. DOI: 10.1016/j.sedgeo.2007.03.007.

Wessel, P., W. H. F. Smith, R. Scharroo, J. Luis, and F. Wobbe (2013). "Generic Mapping Tools: Improved Version Released". *Eos, Transactions American Geophysical Union* 94.45, pp. 409–410. DOI: 10.1002/2013EO450001.

SUPPORTING INFORMATION

Figure S-1 shows the results of 'chequerboard' tests. In these tests synthetic data at sample sites downstream (e.g. white circles in Figure S-1a) are generated using an arbitrary elemental concentration (e.g. Figure S-1a). Concentrations at the 67 downstream samples are then inverted for the composition of source regions (see color map in e.g. Figure S-1a). These tests are performed using the actual sample sites considered in this study and the real drainage networks in the study region. A comparison between the 'actual' source region concentrations and best-fitting results from inverting the 67 sample sites is shown in adjacent panels (e.g. Figure S-1c). As discussed in the body text of the main manuscript, changes in source composition at wavelengths < 20 km are poorly resolved. In contrast, the amplitude and spatial structure of longer wavelength changes in composition are recovered.

Figure S-2 shows the results from applying a low-pass (> 25 km) Gaussian filter to the magnesium data extracted from the G-BASE survey, and to the results of the inverse model (see e.g., Figure 13 of the main manuscript). These results are discussed in the main manuscript.

Figure S-3 – 21 (which are given in the data-repository) show the results from inverting the elemental concentrations of actual samples for source region chemistry. In the main manuscript we show results for Mg and a subset of results for Ca, Rb, V and Be. Figure S-3 – 21 shows the best-fitting inverse model, the G-BASE inventory and comparisons between these estimates of concentration for Ba, Be, Ca, Co, Cr, Fe, K, La, Li, Mn, Ni, Rb, Sr, Ti, U, V, Y, Zn and Zr. The smoothing parameters for each inverse model were determined by systematically varying λ, the optimum values for each element are given in the captions for Figures S-3 – 21. See body text of the main manuscript for details.

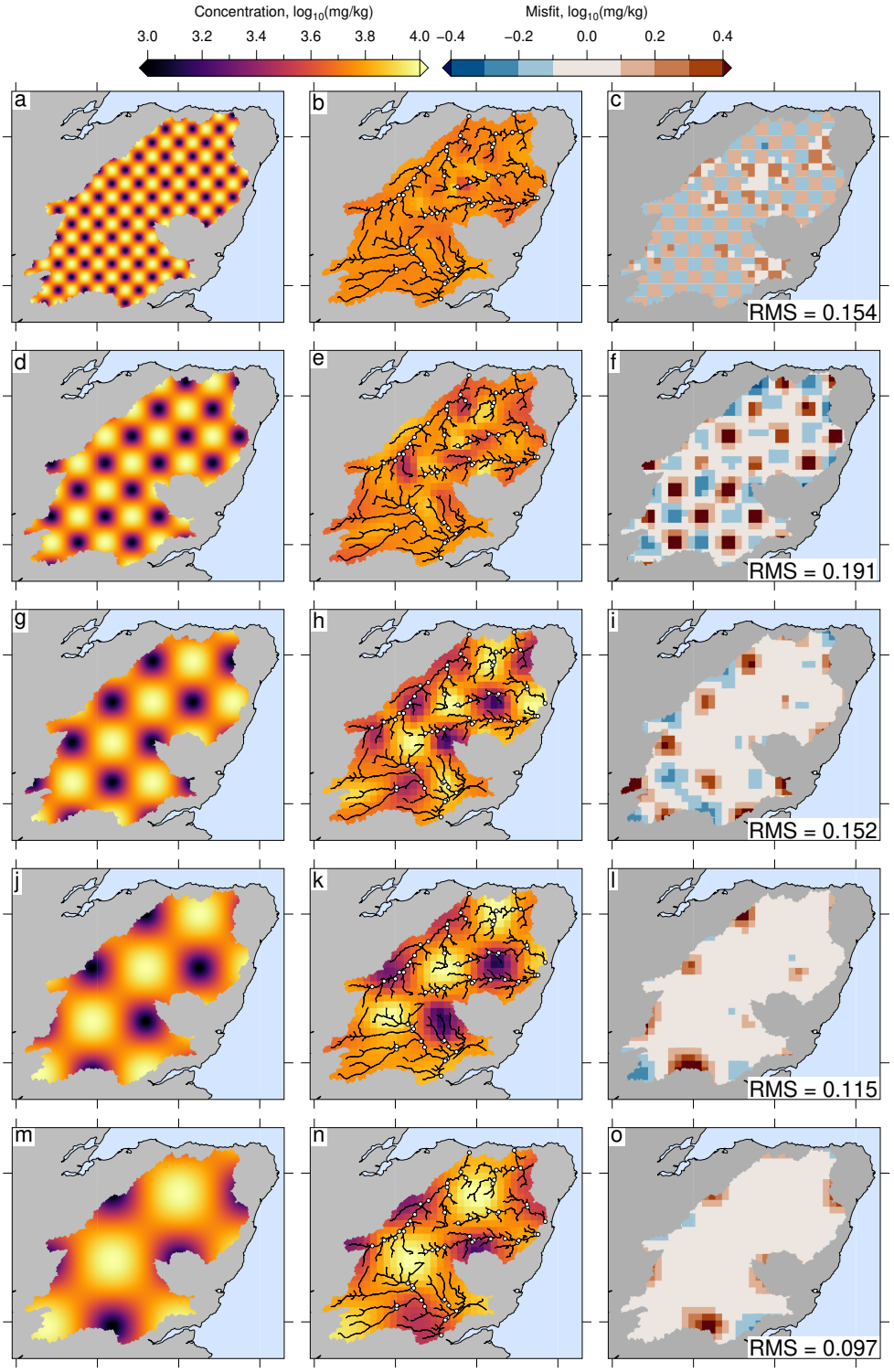

Supplementary Figure 1: **Inverting real downstream sediment samples for concentration of barium in source regions.** (a) Optimum upstream concentration of barium generated by inverting the barium concentration of the 67 samples gathered downstream with smoothing parameter $\lambda = 10^{-0.1}$. (b) Independent G-BASE stream sediment concentration of barium gridded to same resolution as panel (a). (c) Cross-plot of observed (G-BASE) and predicted concentrations for each grid cell (5 km resolution). Colors show misfit discretized at intervals equal to global RMS misfit. Gray dashed line = 1:1 relationship; black line = linear regression. (d) Misfit between observed barium concentration and best-fitting inverse model. Inset indicates distribution of residuals and normal distribution; binwidth = global RMS misfit.

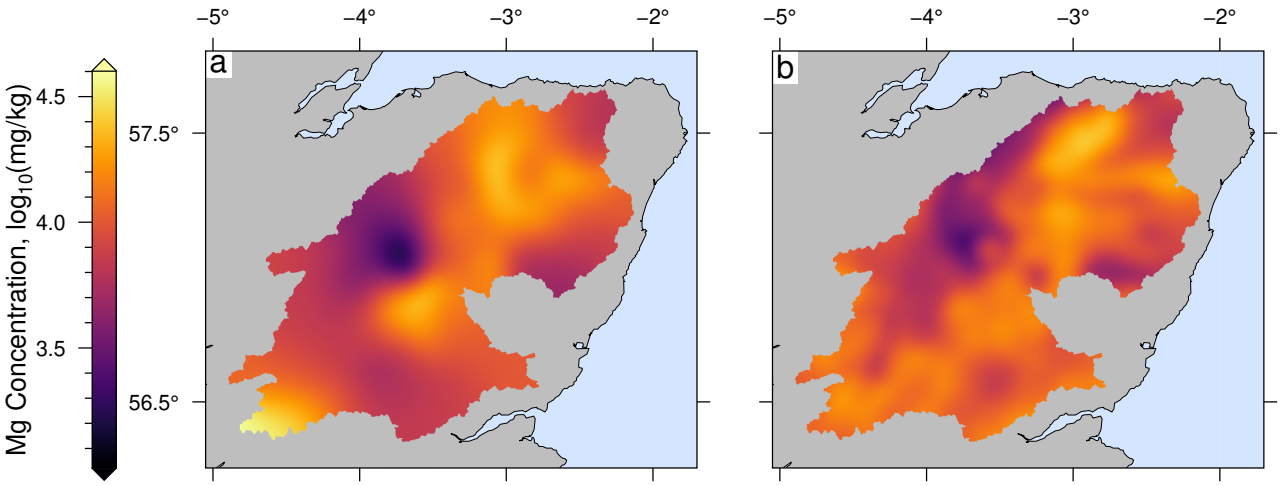

Supplementary Figure 2: **Low-pass filtering of Magnesium.** (a) Best-fitting inverse result for Mg filtered using a 2D Gaussian filter of wavelength 25 km. See Figure 7b of the main manuscript for unfiltered results. (b) G-BASE Mg data filtered using same filter as panel (a). Filtered results for other elements are given in Figure 13 of the main manuscript